CHALMERS
UNIVERSITY OF TECHNOLOGY

Thesis for Master Program
Sustainable Energy Systems
Department of Chemistry and Chemical Engineering

Chromium evaporation and oxidation on a mechanically deformed nano-coated interconnect steel

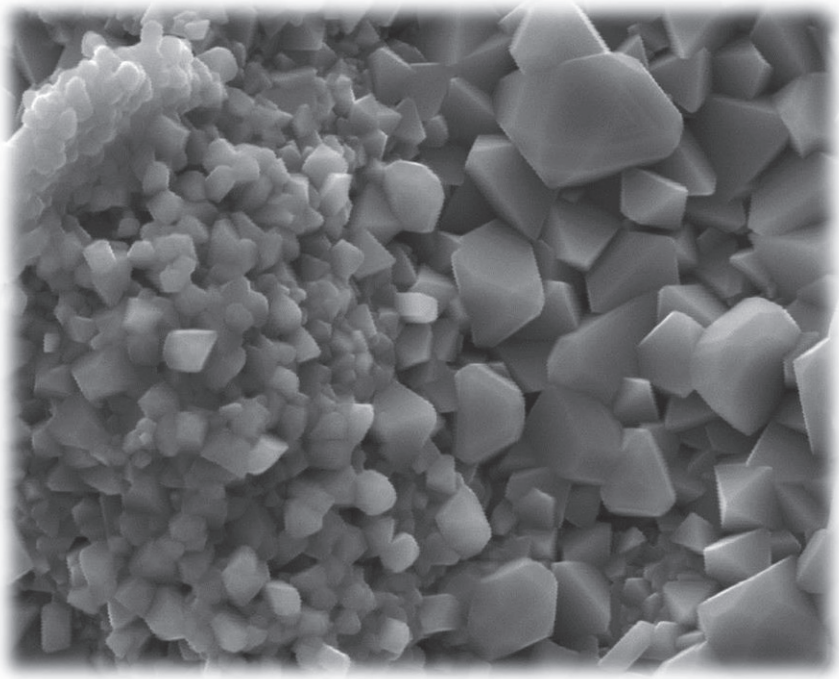

Nikolaos – Ioannis Mertzidis

Supervisor: Hannes Falk Windisch

Examiner: Jan-Erik Svensson

Gothenburg, Sweden 2015

Contents

Abstract

Solid Oxide Fuel Cells (SOFCs) are promising electrochemical devices capable of clean and decentralized power production. Certain interconnect related challenges must be overcome in order for SOFCs to achieve desirable efficiencies during long-term operation and to increase their competitiveness in the energy market. Several stainless steels and state-of-the-art coatings have been investigated for corrosion resistance, mechanical stability and cost optimization of interconnect applications. This study is aimed to investigate the behavior of mechanically deformed AISI 441 steel, pre-coated with a double layered coating of 30 nm Ce and 600 nm Co, exposed in a simulated cathode atmosphere at 850 °C. Chromium evaporation and oxide scale growth was measured in an air-3%H_2O environment using a flow of 6000 sml/min. The effect of uniaxially and biaxially straining as an effect on oxidation and Cr vaporization was studied and compared to a coated material shaped into a real interconnect. The uncoated steel showed poor corrosion resistance, which was greatly improved by the application of a Ce/Co coating. The results for the different deformation levels of pre-coated AISI 441 stainless steels showed similar corrosion properties and Cr evaporation. These were in accordance with the results of the coated, undeformed ones, which suggest that the concept of pre-coating first and then deforming is a feasible option. Surface investigation with SEM confirmed the self-healing of the cracks, formed during mechanical deformation of the coated steel, after one week of exposure.

Acknowledgements

I would like to thank my supervisor PhD student Hannes Falk Windisch, firstly for giving me the opportunity to carry out this thesis and secondly for his endless patience, support and help throughout my work. I would like to thank my examiner Prof. Jan-Erik Svensson for his valuable input and support.

I would like to thank all the members of the Fuel Cell Group, and especially Jan F., Jan G., Rakhsith, Patrik, Mohammad and Christine for their welcoming me to the group, for their help and advice concerning laboratory or theoretical matters, as well as for the inspiring conversations we so often had. I would like to thank Loli and Andrea for their contagious smiles and enthusiasm. Due to all of them the working environment was enjoyable and the experience remarkably rich.

I would like to thank Esa Väänänen and Eric Brunius for their help and technical support. Charlotte and Sandra are acknowledged for their administrative solutions. Last but not least I would like to thank my friends and family for their support and encouragement during all this period.

1. Introduction

Global warming is a major challenge that we have to solve in the near future. Population growth and extensive industrialization have resulted in increased CO_2 emissions, which are mainly responsible for the greenhouse effect. Furthermore, fossil fuel reserves such as coal, oil and natural gas are finite. Therefore, the global energy demand has to be met through new technologies, capable of clean and decentralized energy production. Apart from renewable energy sources, fuel cells are a very promising technology to help in meeting this demand. Fuel cells can convert the chemical energy that is stored in the fuel directly into electricity without combustion [1],[2].

Solid Oxide Fuel Cells (SOFC) are high temperature fuel cells and they reach electrical efficiencies of 60% and are ideal for decentralized heat and electricity production [3]. They can operate on existing fuels via reforming and, hence, the boundaries to their implementation are rather low [2]. However, several material challenges have to be solved in order to allow for a large scale production and implementation of SOFCs. To increase the power of the fuel cell, several cells are stacked together separated by the interconnect material. Among other material related challenges, for example catalysts, interconnects have become an important research area.

Today stainless steels are widely used as interconnect material. Two main obstacles related to ferritic stainless steels as interconnect that have to be overcome for SOFC commercialization are: high temperature corrosion and chromium evaporation. In order to address both issues in a cost efficient way, tailor-made alloys have been developed. Additionally high effective thin film coatings (from sub-µm to µm) can be applied [4]. Since interconnects contribute to a great extent on the total cost of the Fuel Cell stack, an economical alloy with easy manufacturability is desired. Coated interconnect materials can be produced by applying thin metallic coatings prior to stamping into a interconnect shape, which allows for large scale and cost-efficient production. The drawback of this procedure is the cracking of the coatings during the steel deformation.

1.1. Aim

The aim of this thesis was to study the self-healing mechanism of mechanically deformed Ce/Co coated AISI 441. Earlier work by Windisch et al [4] and Bexell et al [5] has shown that thin Co coatings can heal upon exposure. H.F. Windisch et al. [4] has examined the steel Crofer 22 APU, while U. Bexell et al. [5] has investigated a 22% Cr ferritic steel, Sandvik Sanergy HT, both coated with approximately 600 nm Co. In this thesis the much more cost effective steel AISI 441 is studied. Furthermore, this steel is coated with a double layer consisting of both Ce and Co. Pre-coated steel was shaped into a real interconnect and compared to coated materials strained both uni and biaxially.

2. Fuel cells

The basis of the fuel cells is a very simple one. Demonstrated by William Grove in 1839, when he was able the run water electrolysis in reverse. The reactants were hydrogen and oxygen, which recombined will form water. Additionally, current in an external electrical circuit was produced [1]. Another way of looking at the phenomenon is that hydrogen as fuel is being oxidized producing electrical energy and forming water as product.

2.1 Function and principles

A fuel cell consists of three main components: two porous electrodes, the anode and the cathode, and an ion conducting electrolyte. A schematic illustration of a typical fuel cell including the various gas and ion flows is shown in Figure 2.1 [1].

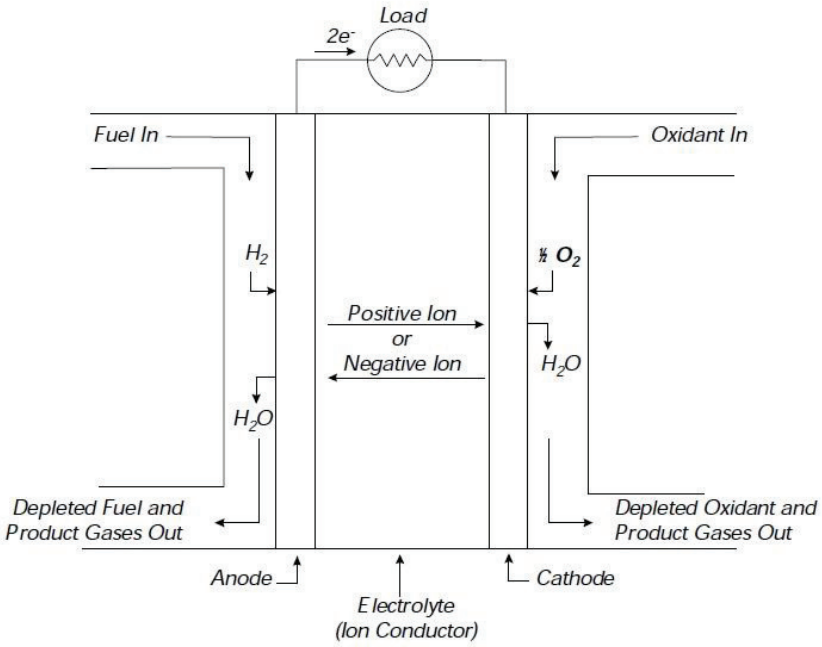

Figure 2.1: Schematic of an individual fuel cell [1]

The fuel and oxidant gases are continuously introduced to the electrodes. Fuel is fed to the anode and the oxidant is fed to the cathode side of the fuel cell. The electrochemical reactions take place at the surface of the electrodes and the electrons are 'drawn' to the external circuit while the mobile ions travel through the electrolyte.

Dependent on the type of the fuel cell, the mobile ion can either travel from the anode to the cathode (hydrogen ion) or the other way (oxygen ion). In the simplest form, a fuel cell is explained by considering pure hydrogen as fuel and oxygen as the oxidant. At the anode, a hydrogen molecule is split into two protons, which are the mobile ions, and two electrons, which produce the current. In the case when hydrogen ions are the mobile ions, protons and electrons will combine with oxygen at the cathode producing water as exhaust emission.

The typical electrochemical reactions that take place if hydrogen is the mobile ion in the fuel cell are listed below.

Anode: $H_2 \rightarrow 2H^+ + 2e^-$ (2.1)

Cathode: $1/2O_2 + 2H^+ + 2e^- \rightarrow H_2O$ (2.2)

Total: $H_2 + 1/2O_2 \rightarrow H_2O$ (2.3)

2.2. Performance

When addressing the performance of the fuel cell, one has to distinguish the ideal performance from the actual one. Ideally a fuel cell's performance is dependent on the electrochemical reactions that take place and it is defined by its Nernst potential, as cell voltage [1]. The Nernst equation for the simplest form of a fuel cell, as described above, is:

Nernst equation: $E = E^o + (RT/2F) \ln [P_{H2} / P_{H2O}] + (RT/2F) \ln [P_{(1/2)O2}]$ (2.4)

2.2.1. Losses

In an operational fuel cell certain losses, or voltage drops, result in a new, actual fuel cell performance. The actual performance is then determined by subtracting the impact of the losses, or voltage drops, that occur in the system. These are: **internal** losses, **activation** losses, **ohmic** losses and **concentration** losses. Each type of fuel cell is described by a different level and extent of these losses and has therefore a different actual performance, with a specific operating power output. The losses are shown in Figure 2.2 [2].

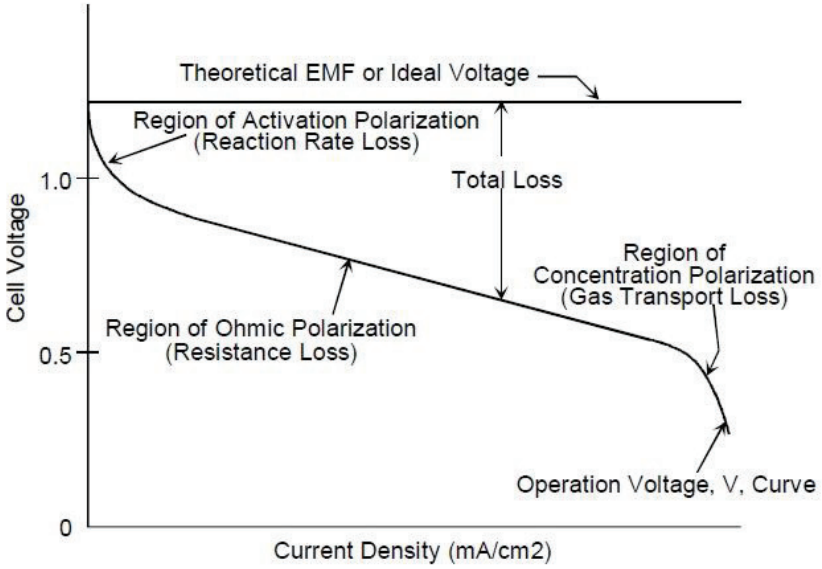

Figure 2.2: Ideal and actual fuel cell voltage/current characteristics [2]

Analyzing the voltage- versus-current graph of a typical fuel cell, three distinct regions emerge. At each region, or current density, different types of losses take place. Every fuel cell type has a different mix of losses and produces a different graph, nevertheless, with distinguishable loss-regions. The internal losses are not visible in the Figure; they refer to the voltage drop from the theoretical electric potential to a lower, actual potential at a current density equal to zero.

2.2.2. Efficiency

The efficiency of an energy conversion device is the amount of useful energy produced in relation to the chemical energy, that takes place when a fuel reacts with an oxidant [1]. In order to compare the fuel cell with the other fuel-utilizing technologies, the ideal efficiency of the fuel cell is defined as:

$$n = \frac{electrical\ energy\ produced\ per\ mole\ of\ fuel}{-\Delta\overline{h}_f} = \frac{\Delta\overline{g}_f}{\Delta\overline{h}_f} \times 100\% \qquad (2.5)$$

The maximum electrical energy available is equal to the change in Gibbs free energy, Δg_f [4]. There are two different values concerning the change in the 'enthalpy of formation', Δh_f and often when addressing the efficiency of the fuel cell, one has to be specific to whether it refers to the *higher heating value* (HHV) or the *lower heating value* (LHV). When this is not mentioned, the LHV is implied [2]. The maximum efficiency of a hydrogen fuel cell, relative the HHV is shown in Figure 2.3.

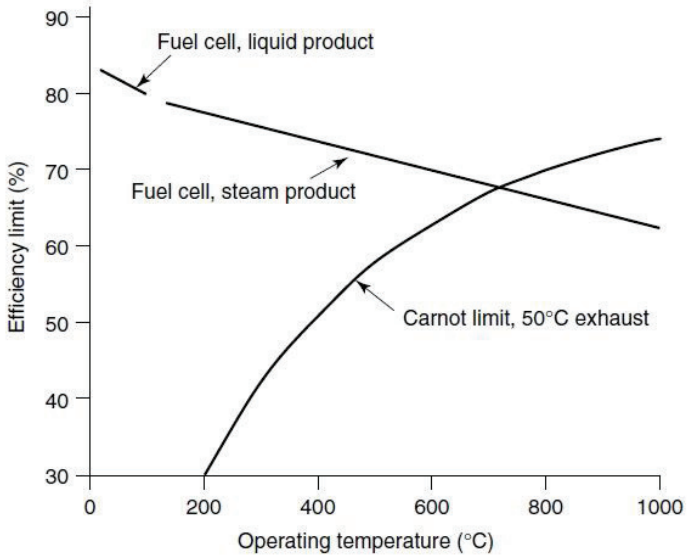

Figure 2.3: Maximum H2 fuel efficiency at standard pressure with reference to HHV, compared with the Carnot limit with 50C exhaust temperature [2]

The graphs in Figure 2.3 represent the maximum efficiency as a function of temperature for a fuel cell and the Carnot limit which is the performance when thermal energy are used as in an internal combustion engine. It should be noted that the graph may be misleading at a first glance, due to the fact that even though the maximum efficiency is higher at low temperatures for a fuel cell, the voltage drops (or losses), as discussed above, tend to take place at low temperatures. On the other hand, at high temperatures the losses are minimized, so in reality, fuel cell voltages are higher at high temperatures. Furthermore, the waste heat generated from the high temperature fuel cells may be used in a *combined heat and power* (CHP) steam turbine system hence; additional useful work will be extracted increasing the total efficiency further.

2.3. Types of fuel cells

The most common types of fuel cells are summarized in table 2.1.

Table 2.1: Types of fuel cells, with respective data [1],[2].

Fuel cell type	Mobile ion	Operating temperature	Applications and use
Alkaline fuel cell (AFC)	OH^-	50-200 °C	Space vehicles, e.g. Apollo, Shuttle
Proton exchange membrane (PEMFC)	H^+	30-100 °C	Vehicles and mobile applications and lower CHP systems
Direct methanol (DMFC)	H^+	20-90 °C	Suitable for portable el. Systems of low power.
Phosphoric acid (PAFC)	H^+	~200 °C	Extended use of 200-kW CHP systems
Molten carbonate (MCFC)	CO_3^{2-}	~600 °C	Medium to large-scale CHP systems up to MW capacity
Solid oxide (SOFC)	O^{2-}	500-1000°C	Varying from several kW to multi-MW capacity. Suitable for all sizes of CHP.

The types of fuel cells are divided into two categories depending on the operating temperature. The two categories are *low temperature* (LTFC) and *high temperature fuel cells* (HTFC). As shown in the table, the HTFC are suitable for high capacity stationary power production, often accompanied with CHP to maximize the energy utilization. LTFC are more suitable for smaller and often portable application or vehicles. In the following chapter, the high temperature fuel cell SOFC will be further investigated.

2.3.1. Fuels for Fuel Cells

Although in principle, hydrogen is referred as the fuel for fuel cells, this is not always the case. Some types require another fuel than hydrogen and have a different tolerance for certain gases. It is not uncommon that some gases can be used as fuel in some fuel cells whereas the same gas is considered a poison for others. Table 2.2 represents the different fuel cells and their relation to some gases [2]. It is significant that HTFC and especially SOFC have a variety of fuels that can be used apart from hydrogen, and that is accomplished with fuel reforming. Moreover, carbon monoxide is a very convenient fuel for SOFC in extra terrestrial atmospheres, as on Mars, where carbon dioxide is abundant and can produce carbon monoxide.

Table 2-2: Fuel requirements for different types of fuel cells [2]

	PEMFC	AFC	PAFC	MCFC	SOFC
H_2	fuel	fuel	fuel	fuel	fuel
CO	poison	poison	poison	fuel	fuel
CH_4	diluent	poison	diluent	diluents/fuel	fuel
CO_2	diluent	poison	diluent	diluent	diluent

2.3.2. Fuel reforming

High temperature fuel cells (HTFC) should generally be considered as complex systems instead of mere fuel cell devices. The amount of waste heat can be utilized in CHP systems as mentioned but it can also be used for fuel reforming. Specifically, the PAFC, MCFC and SOFC must be thought of as an integral part of a complete fuel processing and heat generating system [2]. The idea is that hydrocarbons such as natural gas or biogas, diesel, ethanol, etc, can produce hydrogen through a simple endothermic reaction, thus eliminating any hydrogen supply requirements and excessive storage. The **steam reforming** reaction also produces carbon monoxide, which then through a shift (water-gas) reaction gives carbon dioxide. The steps in steam reforming mechanism are summarized in the reactions:

$$CH_4 + H_2O + \Delta H \rightarrow CO + 3H_2 \qquad \Delta H=206\ kJ/mol \qquad (2.6)$$

$$CO + H_2O + \Delta H \rightarrow CO_2 + H_2 \qquad \Delta H=-41\ kJ/mol \qquad (2.7)$$

The heat from the fuel cell reactions can be used for reforming, and in the case of HTFC there is more heat available than needed. **Internal reforming** is achieved either in the stack (integrated reforming) or directly at the anode (direct internal reforming), where water is produced after the fuel cell reactions, although additional water is needed.

2.3.3. Hydrogen – the ideal fuel

Hydrogen can be characterized as the ideal fuel. It is very light in weight, burns in air with a high temperature (585 °C auto-ignition temperature) and does not produce any carbon dioxide or other greenhouse gas emissions since the only by-product from combustion is water. There are mainly three ways to produce hydrogen: from reforming fossil fuels, biomass and from water electrolysis.

Fossil fuel reforming is the cheapest way and if biofuels are used, then the natural fossil fuel reserves are not compromised. In addition, fuel reforming releases carbon dioxide, which can be assumed as a counter argument for the fuel cell zero-impact properties. Still, reforming is a much cleaner and efficient way to utilize fossil fuels than combustion.

The cleanest way is through water electrolysis. In principle this method is a FC run backwards. The input is electricity and water and the products are hydrogen and oxygen. The implications of electrolysis, is the ability to store the excess power from renewable power production technologies, in the form of hydrogen instead of it going to waste due to lack of demand at the specific time and place the excess occurs. *Solid oxide electrolysis cells* (SOEC) is a very promising technology for hydrogen production [8] and the challenges that must be overcome are the same as in the SOFC and will be further discussed.

Hydrogen storage is a somewhat problematic issue. There are quite many ways to store hydrogen as of now, and promising research is being done in that area. In terms of safety, contrary to what the majority believes, hydrogen is safer than other (fossil) fuels due to its very low weight. In case of an accident, it would burn upwards with lower risk of devastating explosions or residual fire as is the case, for example, with natural gas or diesel.

3. HTFC – SOFC

3.1. Principles and schematics

The Solid Oxide Fuel Cell is a solid-state electrochemical device that uses an oxygen-ion-conducting electrolyte and mixed-conducting electrodes [9]. The solid electrolyte eliminates the need for complicated electrolyte management which is often necessary in the other types of fuel cells. The high operating temperature of >600°C makes it possible for internal fuel reforming and eliminates the need for precious metals such as Pt, since it promotes rapid kinetics. On the downside, the high operating temperature sets high requirements on materials. The production of low cost materials that withstand the high temperature-related problems is the key challenge for the SOFC technology.

The working principles along with the electrochemical reactions that take place at the electrodes of the SOFC are shown in Figure 3.1 [1]. Apart from hydrogen, almost any carbon containing fuels can be utilized as fuel in a SOFC such as diesel, natural and biogas, ethanol, methane and even carbon monoxide [2]. When CO is used as fuel, it is either directly oxidized as shown in Figure 3.1, or it can go through a water gas shift reaction (2.7) and release hydrogen. The released electrons are transferred through the external circuit to the cathode. At the cathode, oxygen (from the air) takes these electrons and is reduced to oxygen ions. The formed oxygen ions diffuse through the electrolyte, driven by a concentration gradient and react with the respective fuel at the anode.

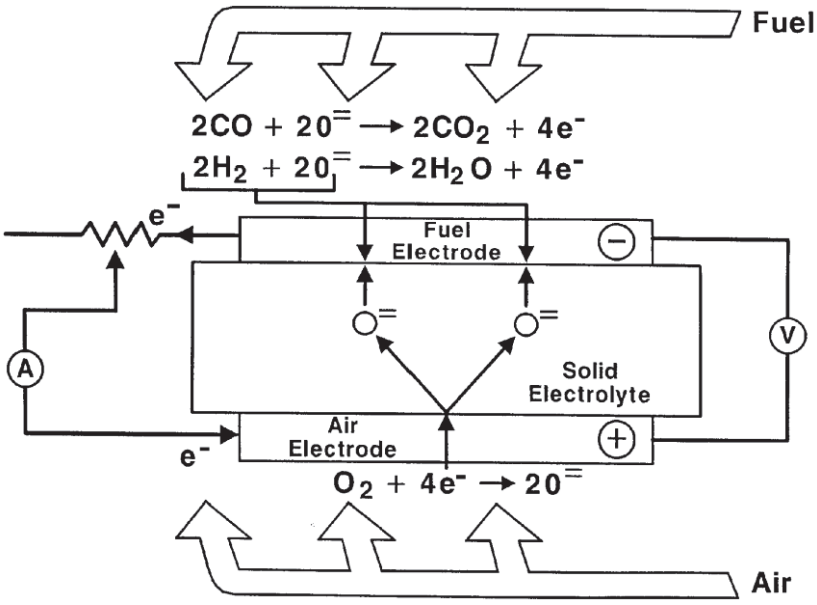

Figure 3.1: SOFC schematic and electrochemical reactions [1]

3.2. Cell components - Materials

3.2.1. Electrolyte

The electrolyte must be conducting for ions and non-conductive for electrons and it has to be stable in both oxidizing and reducing environment [10]. The most common electrolyte materials are *yttria-stabilized zirconia* (YSZ) and *gadolina doped ceria* (CGO), with YSZ as the most widely used. The zirconia is highly stable in both oxidizing and reducing environments. The ability to conduct oxygen ions well is due to the fluorite crystal structure of zirconia and the replacement of Zr^{4+} by Y^{3+} ions. The substitutuion leads to the formation of oxide ion vacancies where the oxygen ion transport can occur [2]. Electrolyte structures of approximately 10 µm thicknesses can be fabricated most often by Screen-Printing.

3.2.2. Anode

The anode must be stable in reducing environments at high temperatures. It is the electrode at which fuel is fed in the fuel cell and simultaneously where the product is formed. It must therefore be able to oxidize the fuel. It must be porous in order to allow for gas flow as well as to increase the surface area therefore the porosity must be maintained throughout the cell's lifetime. Suitable materials for SOFC anodes are nickel, cobalt or precious metals. Due to the high price of cobalt and precious metals, the material of choice is nickel combined with YSZ skeleton to form a Ni-YSZ cerment. The role of zirconia is to hinder the sintering of the metal particles and to ensure an even thermal expansion with the electrolyte. The porosity of the anode is 20-40 vol% ensuring a good mass transport of fuel and product gases [2].

3.2.3. Cathode

The cathode is the electrode at which oxygen is fed as the oxidant agent. Similar to the anode, the cathode must fulfill a number of requirements. It must allow rapid mass transport of reactants and product gases and has to be both ionic and electronically conductive. It must be highly catalytically active with oxygen reduction and minimally reactive with the electrolyte and interconnect materials. The most common SOFC cathode material today is lanthanum magnetite, often doped with strontium to reach the desired electrical conductivity and thermal expansion coefficient [2].

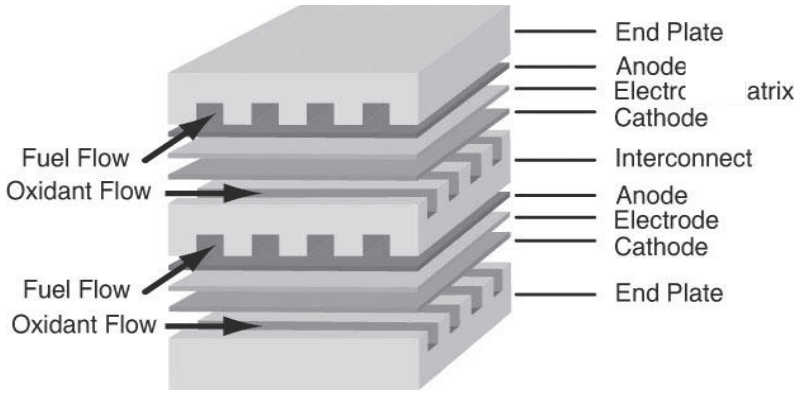

Figure 3.2: Schematic of a SOFC stack

A single fuel cell produces a negligible electrical potential, therefore multiple cells must be arranged together in order to produce the desired power output. The fuel cell stack consists of individual cells connected in series, with interconnects (also called bipolar plates) as the connecting part, as shown in Figure 3.2.

3.3. Interconnects

The interconnect is the part responsible for two main functions: Separating the anode side from the cathode side of two adjacent cells and providing electrical contact between them. Thus, the interconnect material must have high electronic and low ionic conductivity, be stable in both anode and cathode environments, have a compatible thermal expansion with the rest of the fuel cell components. Earlier versions of SOFC operated at higher temperatures (1000°C). In those cells lanthanum chromite ($LaCrO_3$) was used as interconnect material, however since the operating temperature has been decreased have they been replaced with ferritic steels. The latter have several advantages compared to ceramic interconnects, such as lower material and fabrication costs, easier to shape into interconnects, higher electrical and heat conductivity and higher mechanical stability.

3.3.1. Ferritic stainless steels

The most essential requirement for steels as interconnects is high temperature corrosion resistance in both anode and cathode environments. High temperature corrosion resistance is achieved by the formation of a protective oxide layer at the surface during exposure at high temperature separating the atmosphere from the metal. The oxide layer however must be chemically compatible with the electrodes and provide as high as possible electronic conductivity. Ferritic stainless steels that are used as interconnects contain 16-26 %wt chromium. Between that range, the steels that have shown best results and developed for SOFC applications contains approximately 22 %wt. Cr. Some of those specially developed steels are Crofer 22 APU and Crofer 22 H from ThyssenKrupp VDM, Sandvik Sanergy HT from Sandvik Materials Technology and ZMG 232 G10 from Hitachi Metals. They have been optimized for corrosion resistance, chromium evaporation and mechanical properties. The investigated materials and the interconnect related challenges will be discussed in the following chapters.

4. Oxidation theory

Corrosion is the gradual destruction of materials by a chemical reaction with the environment. It can be classified into atmospheric corrosion, which occurs in air at ambient temperatures with the presence of an electrolyte (such as adsorbed water), aqueous or liquid corrosion and high temperature corrosion which is the one that is considered in the applications of SOFC. The most common type of high temperature corrosion is oxidation of metallic material where temperature is an important parameter and determines the corrosion rate.

4.1. Basic thermodynamics

The oxidation reaction of a metal M with oxygen is:

$$xM(s) + y/2\ O_2\ (g) \rightarrow M_xO_y(s) \tag{4.1}$$

The question of whether or not a metal oxide is stable in the exposure environment can be answered by the second law of thermodynamics. If the conditions at high temperature reactions is constant temperature and pressure, the second law can be written in terms of the Gibbs free energy of a system G', where H' and S' is the enthalpy and the entropy of the system [12].

$$G' = H' - TS' \tag{4.2}$$

The Gibbs free energy change of a process will have the following characteristics:

If $\Delta G'<0$ then spontaneous reaction is expected
If $\Delta G'=0$ then the process is at equilibrium
If $\Delta G'>0$ then the reaction is non-spontaneous.

For a chemical reaction (4.3), $\Delta G'$ is expressed as following (4.4):

$$aA + bB \rightarrow cC + dD \tag{4.3}$$

$$\Delta G' = \Delta G^o + RT \ln\left(\frac{a_C^c a_D^d}{a_A^a a_B^b}\right) \tag{4.4}$$

ΔG^o is the free energy change when all the species are in their standard state, and a is the activity of a substance. Gases can be represented in terms of partial pressure, where p_i is the partial pressure of a gaseous species i and P_i^0 represents the pressure in the standard state [12].

$$a_i = \frac{p_i}{p_i^0} \tag{4.5}$$

The standard free energy change for such a system can thus be written as (4.6) and at equilibrium the equation is reduced to (4.7):

$$\Delta G^o = c\Delta G_C^o + d\Delta G_D^o - a\Delta G_A^o + b\Delta G_B^o \tag{4.6}$$

$$\Delta G^o = -RT \ln\left(\frac{a_C^c a_D^d}{a_A^a a_B^b}\right) \tag{4.7}$$

The equilibrium of a system is reached when the Gibbs free energy of that system is minimized [11]. The Ellingham/Richardson diagram in Figure 4.1 can be used to predict whether or not the oxide

formation of a metal will occur and if so, which oxides will form at an alloy at a certain temperature and partial pressure. More stables oxides are plotted in the lower part of the diagram.

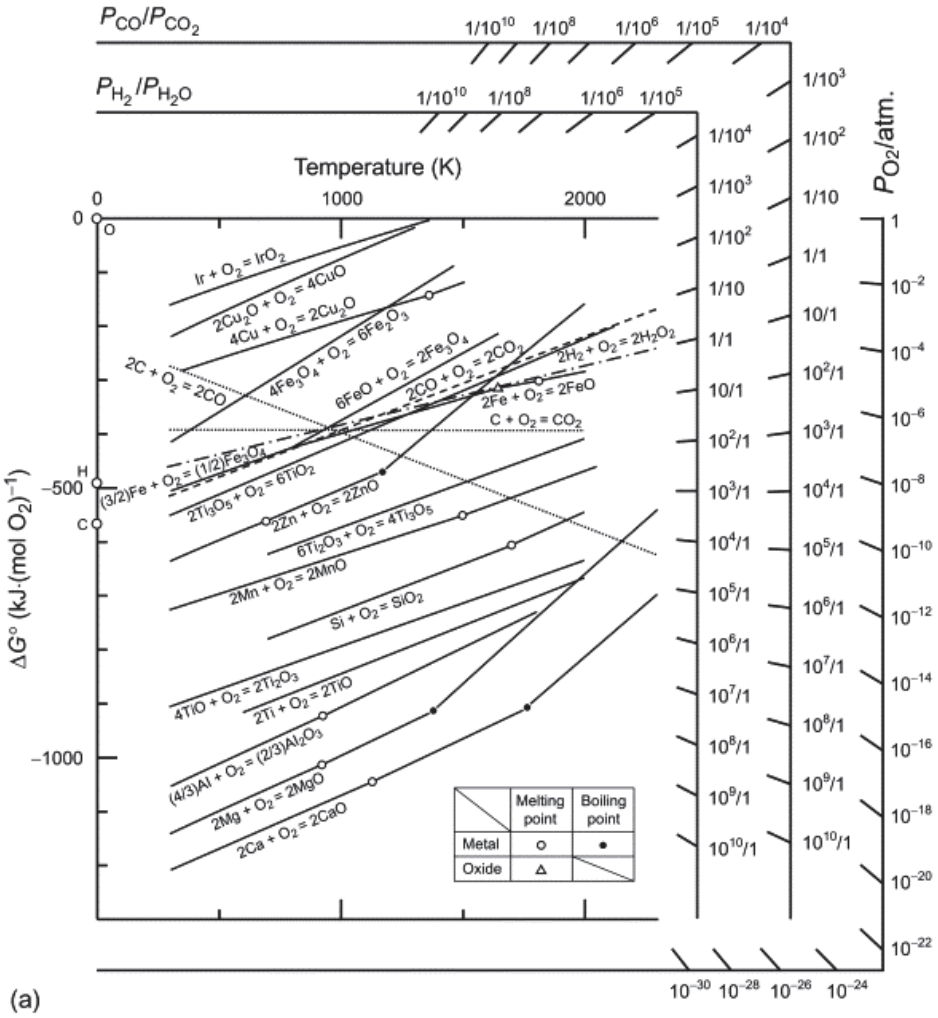

Figure 4.1 Ellingham/Richardson diagram for some metals and the respective metal oxides taken from [14]

4.2. Oxide formation

The initial oxidation process at high temperature can be divided into three steps as shown in Figure 4.2. [13]

1. The adsorption and dissociation of oxygen from the environment onto the surface, charge transfer and O^{2-} formation.
2. Formation of oxide nuclei, which grow to form a continuous scale.
3. Further growth of the oxide scale, while the metal is fully separated from the atmosphere.

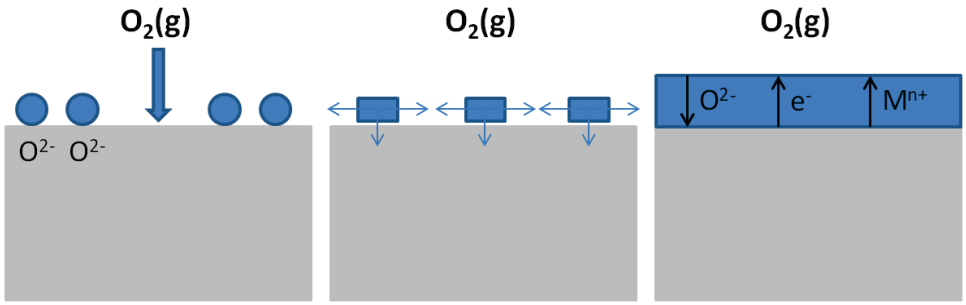

Figure 4.2: Step-wise schematic of the oxide scale formation (adsorption and nucleation) and growth of the oxide scale.

The first steps occur very fast and the surface reaction are rate determining. After the second step is complete, a continuous oxide film covers the surface. At the third step the oxide growth continues through solid state diffusion of either (or both) anions (oxidant) or cations (metal ions). At this point the diffusion process though the oxide becomes the rate determining step. The oxide growth during the last step is strongly temperature dependant. At high temperature the growth rate is significantly higher than at room temperature where it is negligible, as long as diffusion of ions is the rate limiting step.

4.3. Oxidation Kinetics

The rate at which the reactions take place is described by the oxidation kinetics and these are commonly characterized be gravimetric analyses. According to the oxidation process, three different oxide growth behaviors are distinguished: linear, parabolic and logarithmic behavior. The curves for the different mechanisms are presented in Figure 4.3.

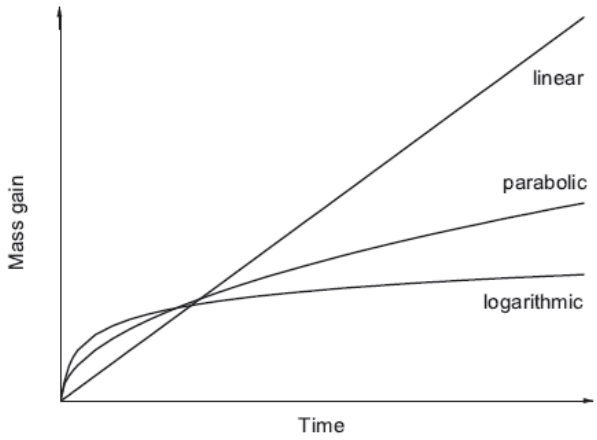

Figure 4.3: Mass gain curves for the three oxidation mechanisms [7].

4.3.1. Linear rate law

During a linear oxide scale growth, the oxidation rate is constant with respect to time and is independent of the gas or metal that is consumed. The linear growth is visible at the initial stages of oxidation and the rate determining step is surface or phase boundary reactions [13]. Linear growth is described by equation (4.8), where x is the oxide scale thickness, k_l is the linear rate constant and t is time.

$$x = k_l * t \tag{4.8}$$

4.3.2. Parabolic rate law

The parabolic oxidation mechanism depends on solid state diffusion and is therefore commonly observed at high temperatures. The theory has been introduced by C. Wagner and it is assumed that the diffusion of ions and electrons is the rate determining step for the growth of the oxide scale. In addition, the reactions are rapid at the phase boundaries and there are local thermodynamic equilibria at the metal-oxide and oxide-air interfaces. Since the growth rate is dependent on the diffusion through the oxide scale, it will decrease with time, as the scale will grow thicker and the diffusion paths will be longer. Thus the oxide thickness increases following a parabolic curve through time and is described by equations (4.9) and (4.10)

$$\frac{dx}{dt} = \frac{k_p}{x} \tag{4.9}$$

$$x = k_p\sqrt{t} \tag{4.10}$$

Where the thickness x increases proportionally to the square root of time t. The constant k_p is the parabolic rate constant and is proportional to the diffusivity of the rate determining ionic species.

4.3.3. Logarithmic rate law

The logarithmic growth mechanism takes place normally at lower temperatures, below 400°C, and after a rapid initial growth, the reaction rate drops to very low levels [13].

$$\frac{dx}{dt} = \frac{1}{t+t_0} \tag{4.11}$$

$$x = k\log(t + t_0) \tag{4.12}$$

Since the mechanism occurs at lower temperatures only a qualitative description of several interpretations can be given, namely; due to the adsorption of reactive species, the effects of electric fields across the oxide layers, progressive blocking of diffusion paths or cavity formation within the oxide layer [13].

4.4. Interconnect-related challenges

Ferritic stainless steel interconnects for SOFC applications face the following challenges: Gradual degradation due to corrosion, chromium evaporation which contributes to cathode poisoning and increased electrical resistance between the interconnect and the electrodes due to the growing oxide scale. Optimizing the alloy is not enough to suppress chromium evaporation hence additional coatings have been proven to be beneficial [21]. The focus of the thesis will be on the cathode side of interconnect (air side).

4.4.1. Corrosion

On the cathode side, the interconnect is exposed to air which contains a small amount of water vapor (a few percent). For corrosion resistance, alloys depend on the well adherent, protective oxide scale that is slowly growing at the surface of the interconnect. Due to the electronic conductivity of Cr_2O_3, chromia-forming alloys have become the material of choice for SOFC interconnects. The protective chromia layer will continuously grow as long as there is sufficient chromium in the metal to support the formation of Cr_2O_3. After extensive chromium oxidation and volatilization, chromium content reaches a certain limit in the metal bulk and fast breakaway corrosion can take place [12]. Therefore, too thin plates should be avoided in order to maintain a sufficient chromium reservoir in the interconnect. Finally, spallation of the oxide scale can be observed. Usually that occurs due to poor adhesion between the oxide scale and the metal, mismatch of thermal expansion coefficients or growth stresses during oxidation.

4.4.1.1. Effect of Reactive elements

Reactive elements, usually rare earth elements such as cerium (Ce), lanthanum (La) and yttrium (Y) can be added to enhance their corrosion resistance of alumina or chromia forming alloys [15]. Even in small quantities, reactive elements can show significant results in corrosion resistance. The principle is that atoms with high mass and high oxygen affinity are beneficial for protecting the alloy against corrosion [16], however there is no clear consensus behind the mechanisms of the effects of reactive elements. Several mechanisms are proposed to explain benefits of reactive elements. The effects that are evident are: change in the oxide scale growth rate, enhancing of the adhesion between the oxide and the substrate and the change in oxygen vacancy diffusion.

4.4.2. Chromium evaporation

The formation of Cr(g) is thermodynamically allowed at high temperatures, however, when oxygen is present a passive oxide, CrO_3(s), is formed and consequently, in presence of oxygen and water vapour, volatile species are produced, such as CrO_3, $CrO_2(OH)$ and $CrO_2(OH)_2$ according to the following reactions:

$$\frac{1}{2}Cr_2O_3(s) + \frac{3}{4}O_2(g) \rightarrow CrO_3(g) \quad (4.13)$$

$$\frac{1}{2}Cr_2O_3(s) + \frac{3}{4}O_2(g) + H_2O(g) \rightarrow CrO_2(OH)_2(g) \quad (4.14)$$

$$\frac{1}{2}Cr_2O_3(s) + \frac{1}{2}O_2(g) + \frac{1}{2}H_2O(g) \rightarrow CrO_2(OH)(g) \quad (4.15)$$

Ebbinghaus [17] has proposed that the predominant volatile chromium specie formed in air containing water vapor, is the chromium oxyhydride $CrO_2(OH)_2$ according to (4.14). Chromium evaporation depends on various factors, such as temperature, water content and oxygen pressure. Another factor that increases the chromium evaporation in SOFC is the fact that due to high air flows, air is constantly renewed, thus a chromium saturated gas environment can't be reached. The lack of equilibrium leads to increased chromium evaporation until the reaction kinetics become the rate limiting mechanism.

4.4.2.1. Protective coatings against chromium evaporation

Chromium evaporation can be significantly reduced by the application of coatings. The main types studied in the literature can be classified into two categories: Perovskite or Spinel type where spinel type coatings may be metallic coatings turned into spinel type oxides upon oxidation. An example of perovskite coating is a $(La,Sr)MnO_3$ slurry, dip-coated on the alloy and sintered in reducing environment [18]. This type of coatings are usually applied thick, however, they suffer from poor adhesion to the metal substrate. Most spinel type coatings used to reduce Cr vaporization in SOFC are based on cobalt combined with the transition metal manganese to result in a cobalt-manganese spinel type oxide layer on the top of the Cr_2O_3 layer. The spinel type coatings canalso be divided into two categories: conversion coatings and oxide coatings. Conversion coatings refer to the application of metal coatings which upon exposure at high temperature are converted into oxides whereas oxide coatings are coatings that are deposited as spinel oxides. Metallic coatings have the advantage that they can sustain deformation without being detached from the substrate. Thin metallic cobalt coatings have proven to decrease chromium evaporation by a factor of 10 compared to uncoated alloys [19].

In Figure 4.4, Froitzheim et.al [21] proposes the evolution of the oxide layer morphology of Co coated samples from the beginning of the exposure up to 3000 h in air at 850°C. At less than a minute of exposure, metallic Cobalt is rapidly oxidized to a spinel type oxide (Co_3O_4) offering a protective layer against chromium evaporation. After one week of exposure, the upper Co_3O_4 has evolved into a $(Co,Mn)_3O_4$ layer. Small amounts of Fe diffuse rapidly into the metallic Co-coating when the material is heated up. The Mn on the other hand is continuously supplied from the steel until the bulk has been depleated. From that time ahead, the upper Cobalt spinel layer remains more or less constant instead further mass gain is attributed to the growth of the inner chromia layer. Thus, the protective properties are maintained since the absence or very small amounts of Cr in the outer layer keeps the Cr evaporation at low rates. On the contrary, uncoated samples form an $(Cr,Mn)_3O_4$ spinel top layer covering the chromia layer, thus decreasing the evaporation of Cr by suppressing the Cr activity at the surface compared to a pure Cr_2O_3 surface. The effect of Ce as a coating should not have an effect on Cr-vaporization as long as the sample is coated with Co. The reason to add the Ce coating is to improve oxidation resistance [21]

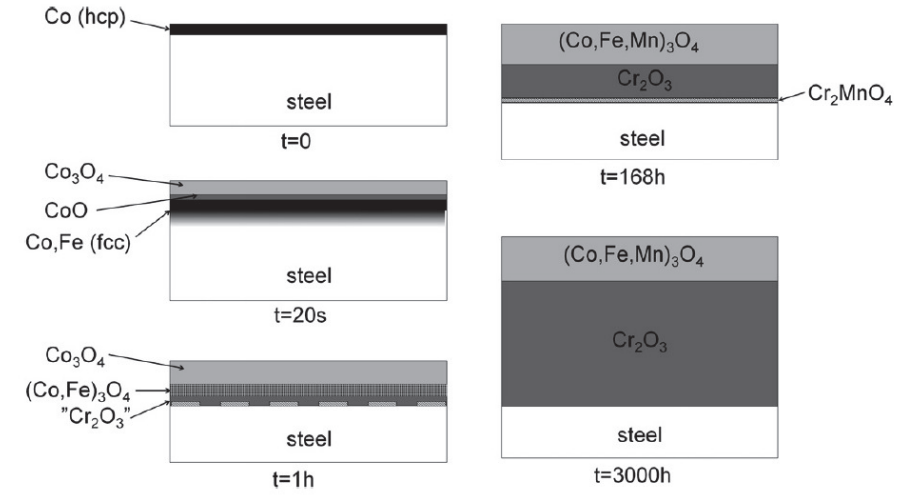

Figure 4.4: Oxide formation morphology at different times up to 3000h [21].

4.4.2.2. Interconnect deformation

To enable gas distribution on both sides as well as to maintain enough contact points with the electrodes to ensure a good electrical connection, the interconnect has to be formed into a certain shape. The deformation process and shape may vary depending on the supplier hence the type of deformation as well as the extent will always vary.

Most coatings today are applied after the steel has been shaped into an interconnect. However by coating the steel with thin metallic films it would be possible to pre-coat steel coils which in a later stage could be deformed at the customer. Large amounts of steel could be coated in one step allowing for much lower coating costs. The main difference between these two options is that in the case of pre-coated and then deformed steel plates, there will be areas where the coating may crack and the metal substrate will be exposed. Post-coating is preferred when the coating can't withstand the mechanical stresses while shaping the bipolar plate. However, in the case of thin film coatings, the protective oxide layer is formed during the priming of the stack and, as it will be further discussed, the micro-cracks that occur have the ability to heal.

5. Materials and Methods

5.1. Investigated materials

The steel of investigation in this thesis was the ferritic stainless steel AISI 441. The composition of the steel is shown in Table 5.1, as given from the manufacturer.

Table 5.1: AISI 441 steel composition.

		Fe	Cr	C	Si	Mn	Nb	Ti	P	Ni
AISI 441	wt. %	bal	17.83	0.012	0.55	0.26	0.48	0.14	0.024	0.13

One type of coating was studied in this thesis. AISI 441 steel was coated with 30nm Ce and 600nm Co. The coating was applied by Sandvik Material Technology AB, by a Physical Vapor Deposition (PVD) technique. To study the effect on oxidation and Cr vaporization as a consequence of mechanical deformation uni and biaxial straining of the coated samples was carried out by Sandvik Material Technology. Moreover, the coated material was shaped into a real interconnect at Topsoe Fuel Cell in Denmark. The thickness of these real interconnects was 0.3 mm. Finally, as already mentioned the extent of deformation will always vary depending on interconnect design and deformation parameters. Therefore, as a more standardized comparison, the material was both uni-axially and bi-axially deformed. The thickness of the uniaxially deformed samples was 0.3 mm (as was the real interconnects) while the thickness of the biaxially deformed ones was 0.2 mm.

The strain level of bi-axially deformed steel was 8%, which was the point just before the fracture of the steel. Three different strain levels have been examined for uni-axial deformation: 10, 20 and 28.1%. The last strain level was the one where fracture was observed. Conclusively, in Table 5.2 below are listed the different samples according to their characteristics:

Table 5.2: Investigated materials.

	Substrate	Coating	Deformation
Uncoated IC	AISI 441		Interconnect shape
Ce/Co Flat	AISI 441	30 nm Ce +600 nm Co	
Ce/Co IC	AISI 441	30 nm Ce +600 nm Co	Interconnect shape
Ce/Co Biax	AISI 441	30 nm Ce +600 nm Co	8 % Biaxial
Ce/Co Uniax	AISI 441	30 nm Ce +600 nm Co	10 % Uniaxial
Ce/Co Uniax	AISI 441	30 nm Ce +600 nm Co	20 % Uniaxial
Ce/Co Uniax	AISI 441	30 nm Ce +600 nm Co	28.1 % Uniaxial

5.2. Sample preparation

All investigated samples except the samples shaped into a interconnect were received as sheets from Sandvik Materials Technology AB. The samples formed into real interconnects were coated at Sandvik Materials Technology and then sent to Topsoe Fuel Cell for the deformation process. Before exposure all materials were cut into coupons of 15x15 mm^2 using a metal cutting tool. The samples were cleaned in an ultrasonic bath, submerged first in acetone and then in ethanol. Subsequently, the samples were weighed using a micro-balance with 1µg readability.

5.3. Exposure techniques

The exposures were carried out at 850°C, in a horizontal quartz tube reactor. The environment of the exposure was similar to that of the SOFC cathode side. The gas flow was set to 600 sml/min, and the air was humidified using either of the following techniques: A heated water wash bulb in combination with either a spiral cooler or a FC™-Series humidifier; a shell and tube moisture exchanger that allows transfer of water vapor (water-to-gas setup). The dew point was set to 24.4°C to ensure 3% water content. The setup of the furnace system is presented in Figure 5.1.

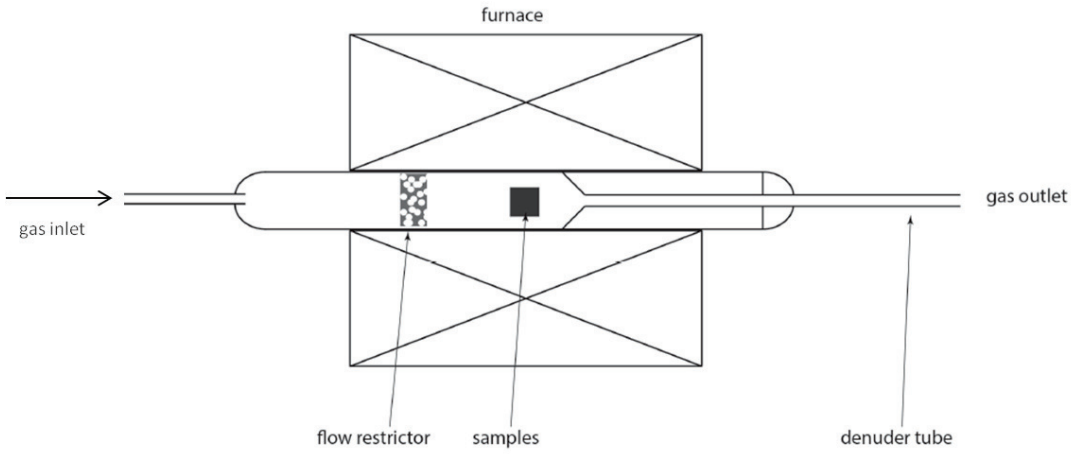

Figure 5.1: Tubular furnace setup.

Two types of exposures were carried out; Isothermal exposures up to 336 h and one long-term exposure. For the long term exposure three coated and three uncoated samples both shaped into interconnects were exposed simultaneously. These samples were discontinuously exposed for 2000 After 2000 h coated and uncoated samples were exposed isothermally (separately) and Cr vaporization was measured. All other exposures where carried out isothermally. For these exposures, three samples of the same materials was exposed simultaneously and Cr vaporization was measured using the denuder technique.

5.3.1. Denuder technique

This method to measure vaporization of Cr species was developed at Chalmers University of Technology. The technique is based on a tubular furnace setup where the denuder tube is mounted on the outlet side of the furnace tube. The inside of the denuder tube is coated with sodium carbonate, prepared by flushing a thick solution of sodium hydroxide and methanol through the denuder which is then dried while carbon dioxide flows through according to the following equation (5.1)

$$NaOH(s) + CO_2(g) \rightarrow Na_2CO_3(s) + H_2O(g) \quad (5.1)$$

As the denuder tube is mounted on the outlet side of the furnace, the exhaust gas is led through it and the volatile chromium species react with the sodium carbonate according to (5.2)

$$CrO_2(OH)_2(g) + Na_2CO_3(s) \rightarrow Na_2CrO_4(s) + CO_2(g) + H_2O(g) \quad (5.2)$$

The denuder is subsequently leached with deionized water and a yellow solution is produced. The chromium concentration (as chromate ions) in the solution is quantified using a spectrophotometer. The collection efficiency of the denuder technique is 95±5% [6]. The denuders were changed at regular intervals to obtain the rate of chromium evaporation as well as the total amount of evaporated chromium at certain times.

5.4. Analytical techniques

The spectrophotometry analyses of the denuder solution where carried out throughout the exposures whereas techniques such as gravimetric analyses, Scanning Electron Microscopy (SEM) and Energy Dispersive X-ray Spectrometry (EDX) were used after exposure

5.4.1. Spectrophotometry

The spectrophotometer is a device that consists of a light transmitter of various wavelengths and a photometer. The solution containing light absorbing ions or molecules is placed between the light source and the photometer. As light is emitted through the solution, a portion of the light is absorbed by the ions in the water solution, in this case CrO_4^{2-}. The rest of the emitted light passes through the solution and is transmitted through to the photometer. At the photometer a voltage is generated, the intensity of which depends on the amount of the light that is absorbed by the ions of the solution. Thus the absorption can be linked to concentration of the ions in the solution. The absorbance can be calculated by the Beer-Lambert law (5.3).

$$A = \log_{10} \frac{I_0}{I} \quad (5.3)$$

Where A is the absorbance, I_0 is the intensity of the transmitted light for a given wavelength through pure solvent and I the intensity of the transmitted light through the solution. The monochromatic light was set to wavelength of 370nm. The spectrophotometer was a Fischer Scientific Evolution 60s UV-Vis equipped with a Xenon flash lamp light source set.

5.4.2. Scanning Electron Microscopy (SEM)

A scanning electron microscope is an instrument that scans the surface of a sample with a focused electron beam. The beam produces signals which are measured and give data about the targeted area of interest. The data that are produced can give information concerning surface topography as well as the elemental composition of the surface. In this thesis the emission signals that were used to image the sample depended on Secondary Electrons (SE) and Backscattered Electrons (BSE). Additionally, EDX was used for chemical analysis of the samples' surfaces. The interaction volume is the volume of the specimen where the respective signal escapes from, and depends on the atomic number of the examined surface. According to the signal that is used, different interaction volume was taken into account.

5.4.2.1. Secondary electrons (SE)

Secondary electrons are the result of inelastic scattering of electrons of the specimen, by incident or backscattered electrons. These electrons have low energies, below 50eV. If the secondary electrons

are released at depths less than 10nm, they are able to leave the specimen and enter the vacuum chamber, where they are captured. Otherwise, if they are released at depths greater than 10 nm, they will be absorbed by an ionized atom and will not exit the specimen volume. Due to their surface sensitivity, secondary electrons provide topographical information about the sample surface.

5.4.2.2. Backscattered electrons (BSE)

Backscattered electrons stem from the electron bean itself, by elastic collision with the atoms of the sample. They have higher energies than secondary electrons. They also have larger interaction volumes (see Figure 5.3), compared to secondary electrons. That leads to a decrease of the topographic contrast and resolution. The number of backscattered electrons is proportional to the size of the atomic nucleus of the specimen. Thus, BSE images can give information regarding variations in the chemical composition of the surface.

5.4.2.3. Energy Dispersive X-ray Spectrometry (EDX)

When the electron beam knocks out an electron of a low-energy orbital of an atom, a high- energy electron of an outer orbital takes its place by falling in a lower energy state. In order to compensate the energy difference, that kind of relaxation leads to X-ray emission. The energy loss, or the X-ray, is characteristic for a specific element. Thus, EDX is useful for elemental identification. For all analyses, a working distance of 12 mm and an acceleration voltage ranging from 10-20 kV were used. The low accelerating voltage was used to reduce the interaction volume since this is rather large for the emission of X-rays as can be seen in Figure 5.3.

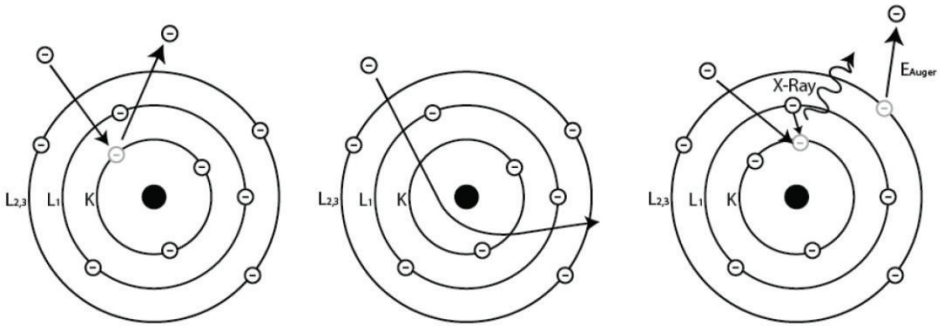

Figure 5.2: Electron atom interactions: SE, BSE and X-rays [23].

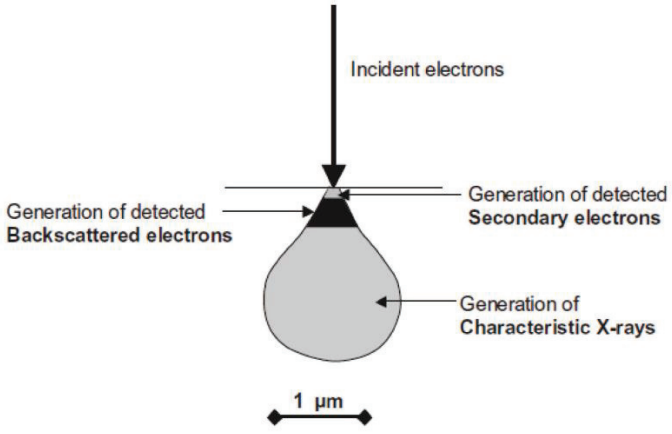

Figure 5.3: Interaction volume of different signals [24].

6. Results

6.1. Mass gain

In order to evaluate the oxidation performance of the steel, gravimetric data have been gathered. According to the samples' mass gain at each time of measure, the mass gain (mg/cm^2) has been plotted. Both continuous and discontinuous exposures were performed at the same conditions; air with 3% water content at 850 °C, with a total flow of 6000 sml/min. Long term, discontinuous exposures were performed for the coated and uncoated IC samples, for 2000 hours. At certain times, the samples were taken out of the furnace, weighed and then placed back in the furnace to resume the exposure. Isothermal, or continuous, exposures were performed for all samples for different time periods, for a maximum of 336 h (2 weeks). Along with the mass gain profiles, the isothermal exposures provided data for Cr evaporation measurements.

6.1.1. Isothermal exposures

Continuous, or isothermal, exposures were carried out primarily for chromium evaporation evaluation and micro structural investigation. However, the samples were weighed before and after exposure, and thus an additional gravimetric profiling was made. The periods of exposure were: 6 minutes, 24 hours, 168 hours (1 week) and 336 hours (2 weeks). For each exposure, three coupons of the same material were used to gain statistical relevance. The results were in accordance with the discontinuous behavior (see Figure 6.3), which indicates that the exposures were performed with minimal flaws.

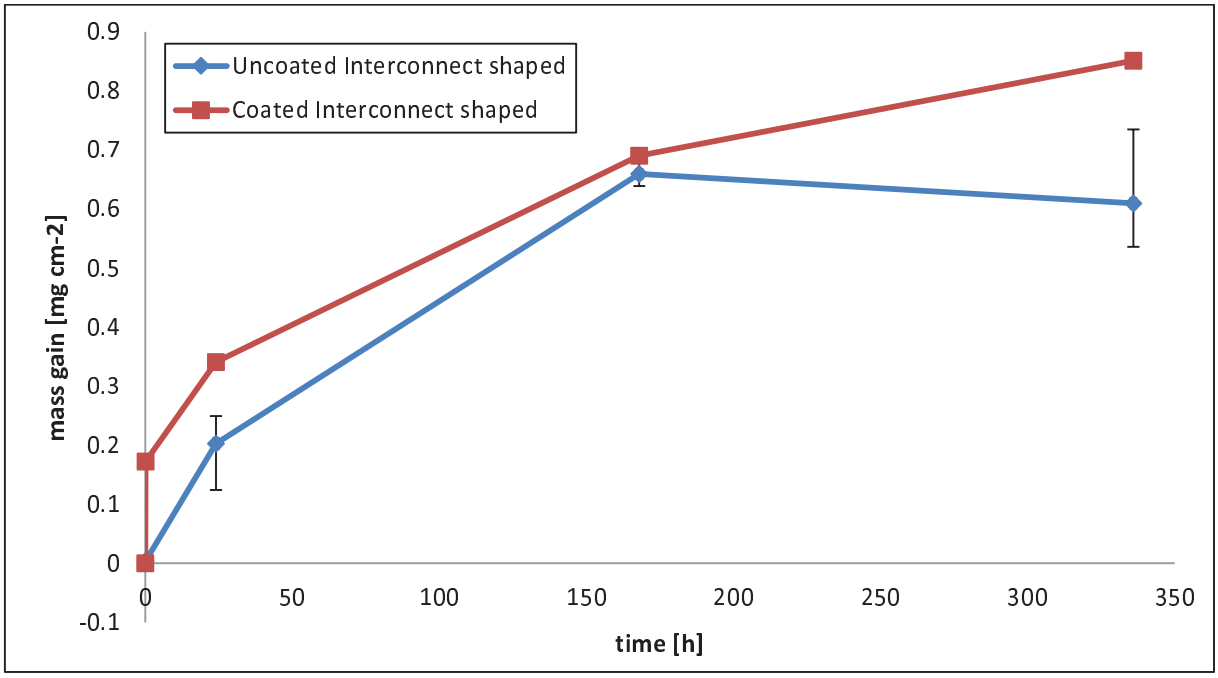

Figure 6.1: Isothermal exposure of coated and uncoated interconnect shaped 441 steel

In Figure 6.1, the mass gain for the uncoated material seems to decrease between 168 and 336 h and that is attributed to spallation as can be observed further down in Figure 6.8. Spallation can also be explained by the deviation that is observed in the mass gain of the three simultaneously exposed, uncoated samples, as indicated by the error bars. The deviation in mass gain is minimal for the coated samples; hence the error bars are almost invisible. In Figure 6.2 the comparison of the uniaxially and

biaxially deformed samples is displayed and compared to the underformed reference material. There, one can see an almost identical growth rate for the maximal uniaxial and biaxial strained steels, while the mass gain of the undeformed steel lies a bit below the deformed ones'.

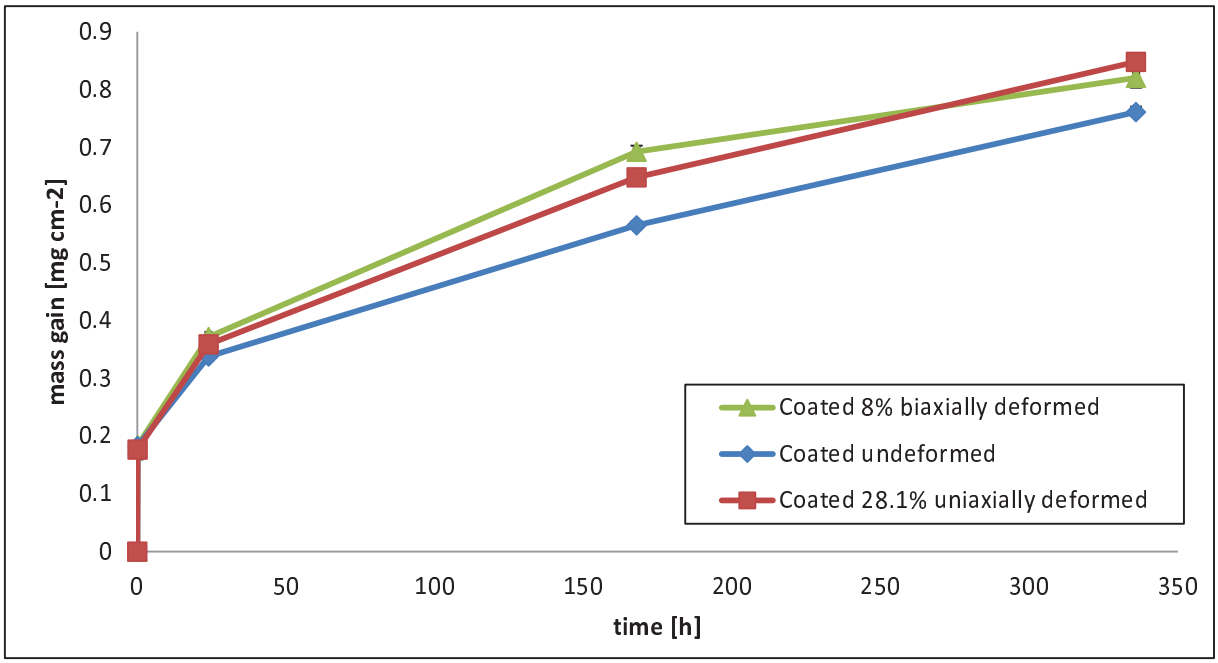

Figure 6.2: Isothermal exposure of uniaxially and biaxially deformed 441, with undeformed reference.

6.1.2. Discontinuous exposures

Long term exposure was performed for the coated and uncoated interconnect shaped 441 steel. Three uncoated and three coated coupons were placed simultaneously in the furnace and exposed for 2132 h without measuring Cr vaporization. After the 2132 h each type of material was further exposure and Cr vaporization was measured (Figure 6.6). As shown in Figure 6.3, the two materials follow an almost parabolic growth mechanism. The uncoated material had a slow oxidation rate during the first minutes of exposure, compared to the coated one, which after six minutes had a mass gain of 0.17 mg/cm^2. This is explained by the rapid oxidation of Cobalt that is applied as coating. After 192 h, the mass gain of the two materials was almost the same. However, afterwards, the oxidation rate of the uncoated steel drops, due to spallation of the oxide scale. The spallation was visible both with naked eye and in the micro-structural investigation, as will be shown in further chapter. The coated samples did not display such behavior, as the oxide scale's adhesion was better. After 2132 hours, the mass gain of the uncoated steel was 1.12 mg/cm^2 and the coated steel was 1.37 mg/cm^2.

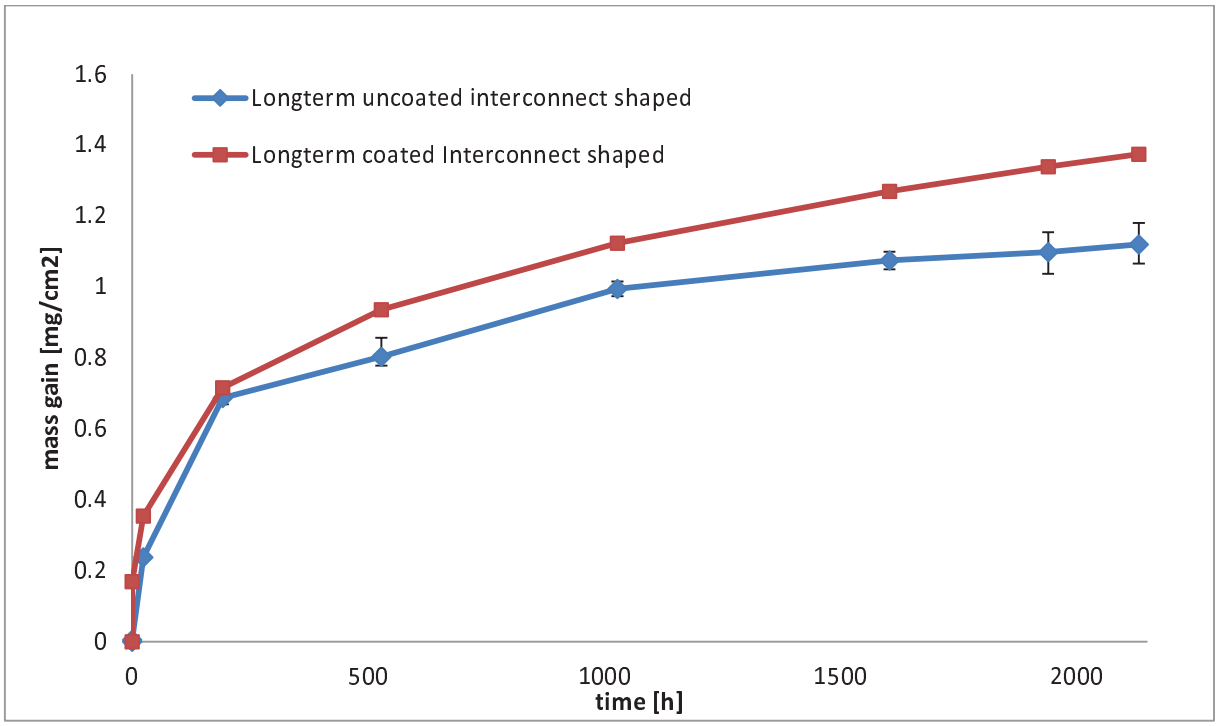

Figure 6.3: Discontinuous gravimetric measurements of coated and uncoated Interconnect shaped 441 samples

6.2. Cr evaporation

Chromium evaporation measurements were performed via isothermal exposures. Separate exposures were performed for the same materials, for each of the aforementioned time periods for microstructural investigation purposes. For the evaluation of the samples regarding Chromium evaporation, plots have been produces for the total accumulated evaporated chromium over time. In most experiments, the denuders were changed on a daily basis. It was observed that the Cr-vaporization data collected during 168 h (1 week) of exposure matched the ones collected during 336 h (2 weeks) exposure. That proved that there weren't flaws in the experimental procedure. Therefore, only the graphs of the 2 week exposures are shown here (Figure 6.4).

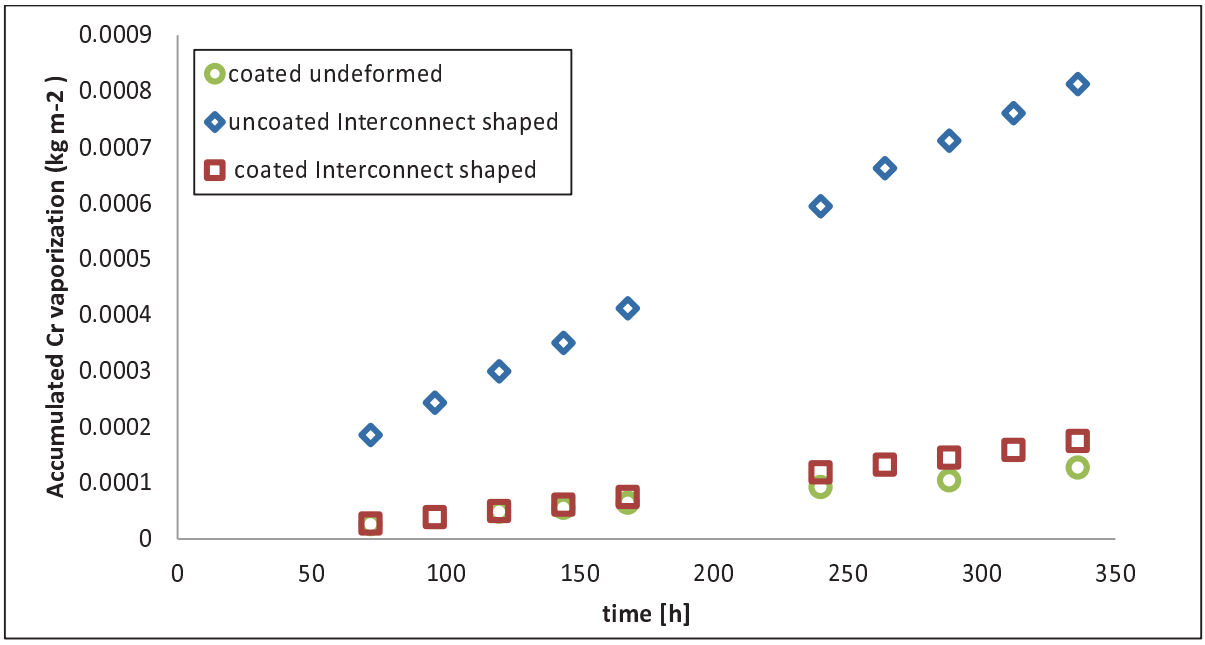

Figure 6.4: Total accumulated evaporated Chromium from coated and uncoated IC shaped, with undeformed reference 441 steel in air 3%-H_2O at 850°C.

In Figure 6.4, the total amount of evaporated chromium for the coated and uncoated interconnect shaped as well as the coated undeformed 441 steel are presented. After 336 h of exposure, the uncoated steel exhibited a significantly higher amount of total evaporated chromium, equal to 0.00081 kg/m^2, compared to both coated materials, namely 0.00017 kg/m^2 for the IC shaped and 0.00012 kg/m^2 for the undeformed.

To further examine the effects of deformation on Cr evaporation, plots have been produced for the uniaxially and biaxially strained materials and are presented in Figure 6.5. For all samples, the Cr evaporation follows almost a linear trend. Regarding the uniaxially deformed steel, all strain levels on the plot show very little difference in Cr evaporation. The biaxially deformed steel follows somewhat lower Cr evaporation, almost identical with the undeformed samples. The lower levels of Cr evaporation for the biaxially deformed samples can be attributed to the thickness of the samples. The area, where the coupons had been cut (edges), acts as an uncoated surface and thus the specific Cr evaporation is significantly higher in this region than from the coated surface. The total uncoated area is however only 4% of the total surface for the 0.3mm thick samples. Since the biaxially deformed samples are 0.1mm thinner, than the rest, slightly lower Cr-vaporization could be expected. Again these differences are very small and does not necessary be due to the deformation process or the thickness difference.

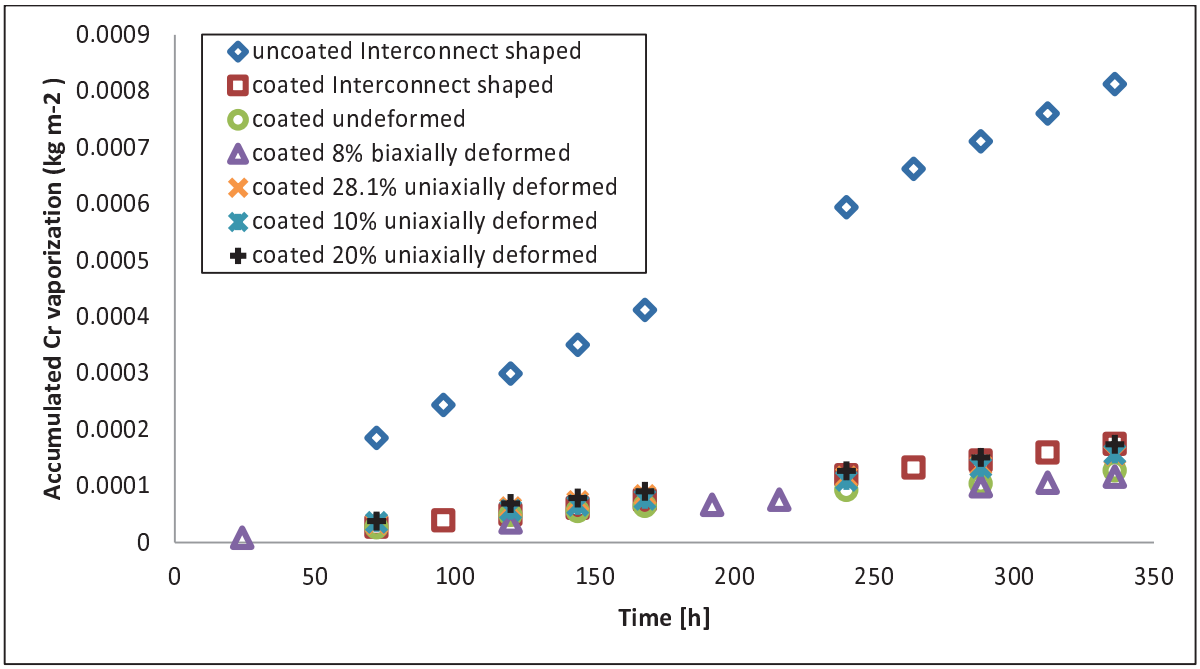

Figure 6.5: Total accumulated evaporated Cr for all samples in air 3%-H_2O at 850°C.

In Figure 6.6, the rate of Cr evaporation is presented for both short (336 h) and long term (>2000 h) exposure. The rate of Cr vaporization for the coated sample was almost identical between 2000-3000 h as after 336 h whereas the rate has increased for the uncoated material.

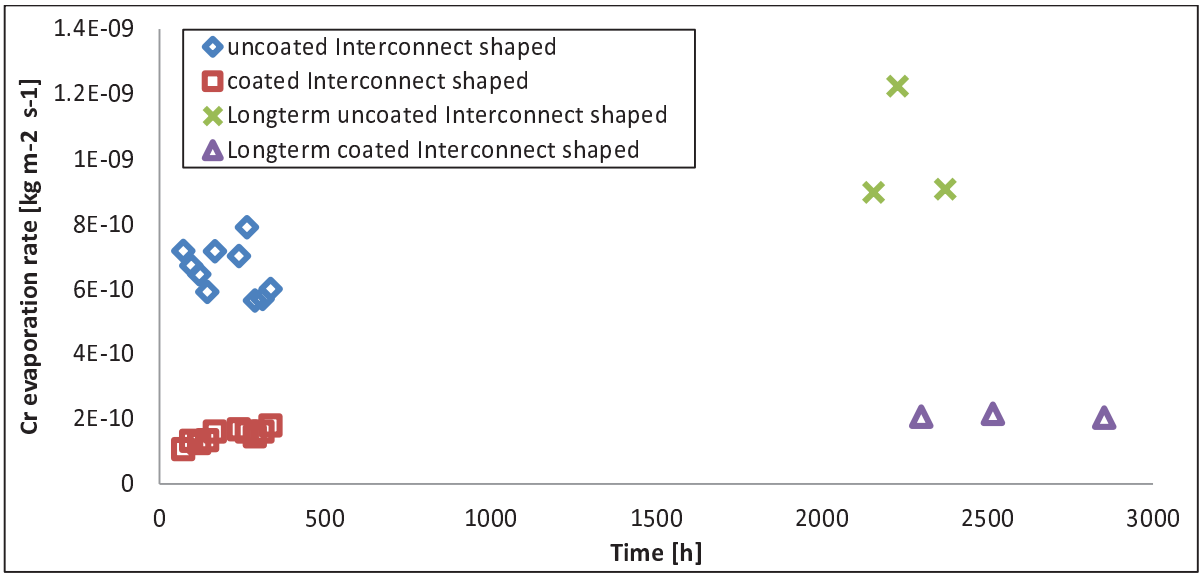

Figure 6.6: Cr evaporation rate for short and long term exposure of uncoated and coated Interconnect shaped samples in air 3%-H_2O at 850°C.

6.3. Microstructural evolution

In order to obtain a better view of the oxidation process, the samples have been investigated using SEM. Top view images have been captured for every material, both before exposure and for different exposure periods. EDX maps have been produced to assess the elemental composition of the top oxide layer over time.

6.3.1. Uncoated, Interconnect shaped samples.

In Figure 6.7, the unexposed, uncoated sample is displayed at 200x magnification. As there is no coating present, crack formation is not expected. In Figure 6.8 the uncoated interconnect shaped samples after 336 hours of exposure can be seen, at 200x and 2000x magnification. The thermally grown oxide layer seems to be vulnerable to cracking and has poor adherence to the metal substrate. Thus, extensive spallation can be observed. The EDX maps, produced with a accelerating voltage of 15kV shown in Figure 6.9 shows that a top layer oxide rich in Cr and Mn was formed. Grolig et al. [20] showed that the uncoated AISI 441 do form a top layer consisting of $(Cr,Mn)_3O_4$ on top of the Cr_2O_3 layer when it is exposed to the same temperature and environment. The middle of the area of spallation is rich in Fe, which depicts the metal substrate.

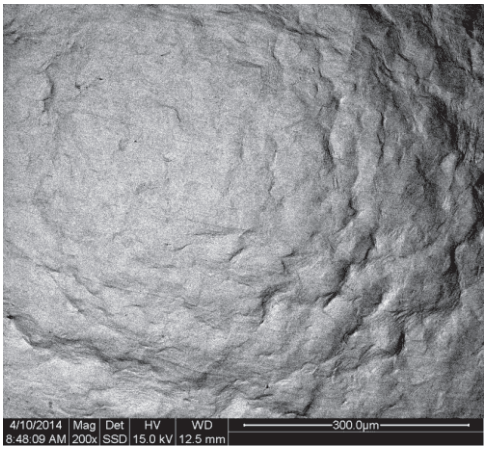

Figure 6.7: Top-view of interconnect shaped, 0.3mm thick, uncoated, unexposed sample; 200x magnification, BSE accelerating voltage 15kV.

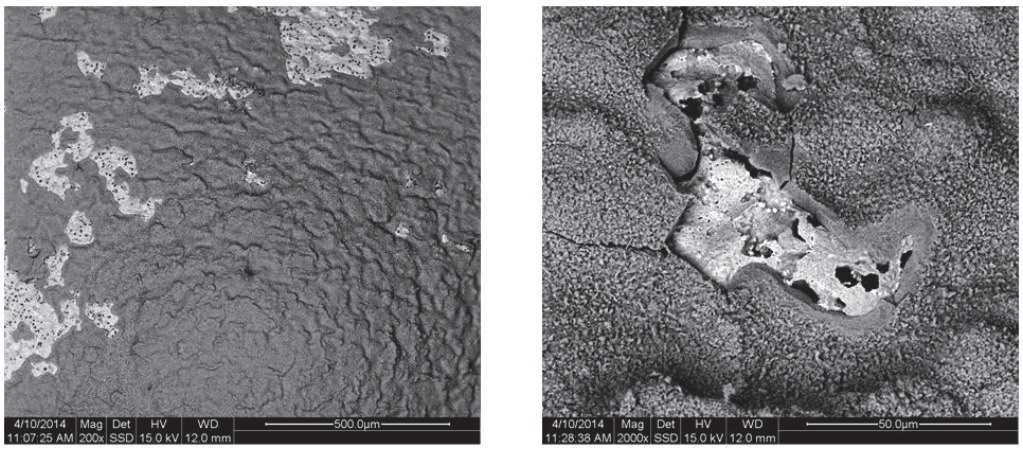

Figure 6.8: Top-view of interconnect shaped, 0.3mm thick, uncoated sample after 2 weeks of exposure; 200x and 2000x magnification, BSE accelerating voltage 15kV.

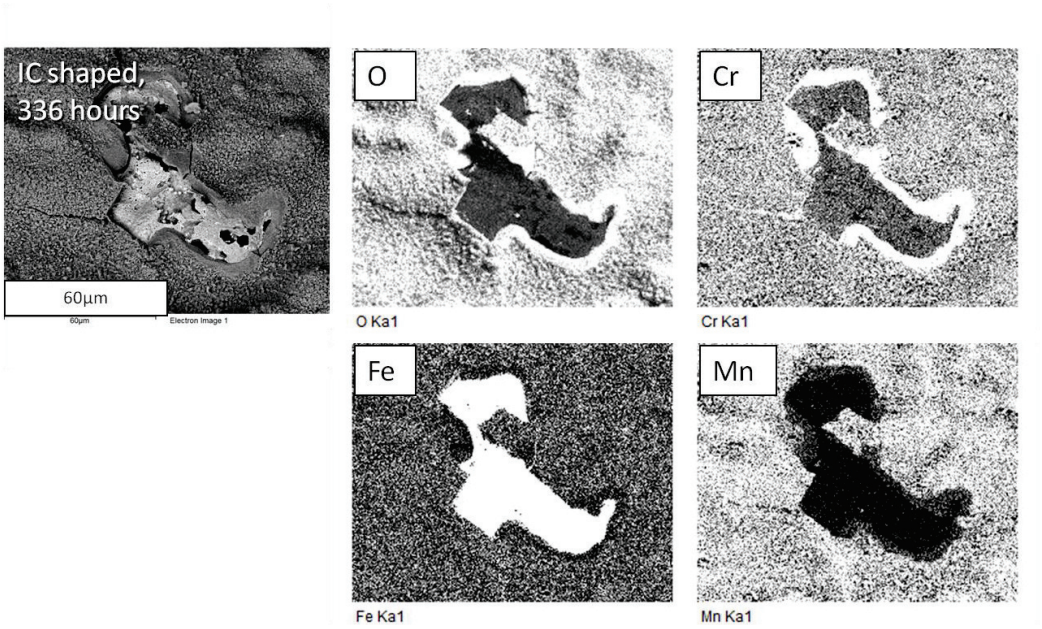

Figure 6.9: EDX maps of the Interconnect shaped, 0.3mm thick, uncoated sample after 2 weeks of exposure, accelerating voltage 15kV.

6.3.2. Coated, undeformed samples.

The unexposed, underformed, 0.3 mm thick, coated sample (reference) in Figure 6.10, shows a uniform thin film coating over its surface. Since the sample is not deformed in any direction, the absence of cracking is expected. The anomalies that are observed on the surface are attributed to the rolling of the metal sheet which was carried out before the coating process. After 336 hours of exposure, as seen in Figure 6.11, a uniform and well adherent oxide layer covers the surface of the sample. The EDX maps, produced with an accelerating voltage of 15kV, (Figure 6.12), shows that the surface is rich in Co and Mn suggesting that most of the surface is covered by $(Co,Mn)_3O_4$.

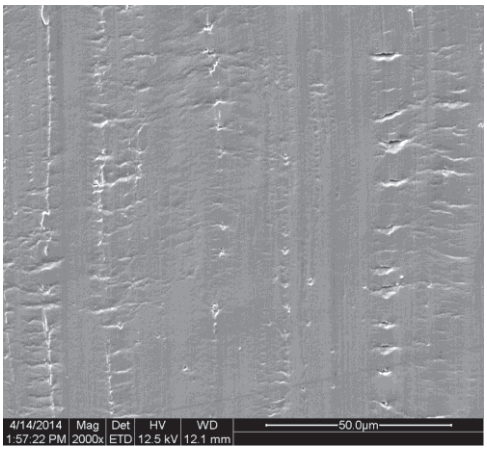

Figure 6.10: Top-view of undeformed (reference), 0.3mm thick, coated, unexposed sample; 2000x magnification, SE accelerating voltage 12.5kV.

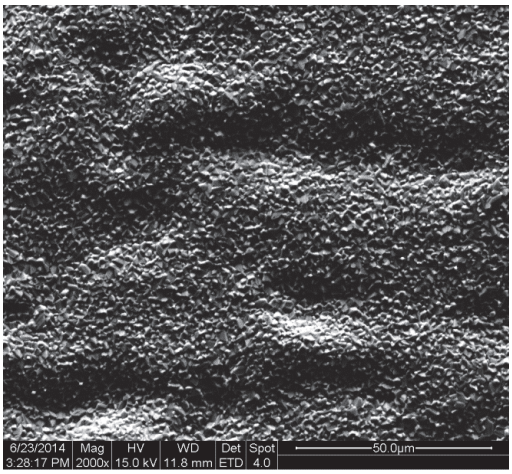

Figure6.11: Top-view of undeformed (reference), 0.3mm thick, coated sample after 2 weeks of exposure; 2000x magnification, SE accelerating voltage 15kV.

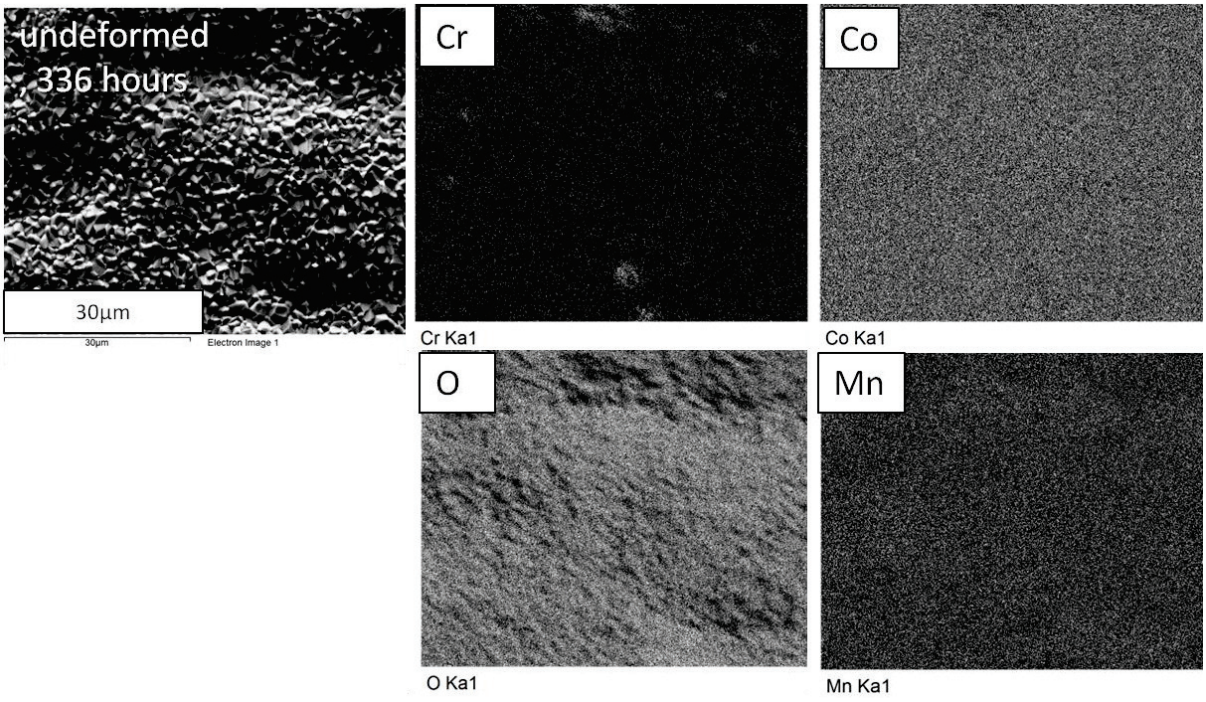

Figure6.12: EDX maps of the undeformed (reference), 0.3mm thick, coated sample after 2 weeks of exposure, accelerating voltage 15kV.

6.3.3. Coated, 8 % biaxially deformed samples

The 0.2 mm thick, 8% biaxially deformed, Ce/Co coated 441 steel was investigated unexposed, after 6 minutes, 24 h, 168 h and 336 h of exposure. The top view images and EDX maps, for different elements, relevant for each stage, will be presented below.

Figure 6.13 shows the top view of the unexposed sample in 2000x magnification. The biaxial deformation process produced cracks in the coating, which run along the two major perpendicular axes. The coating after deformation had a good adhesion to the metal substrate with minimal spallation. The width of the cracks is variable, with a maximum of approximately 5 µm.

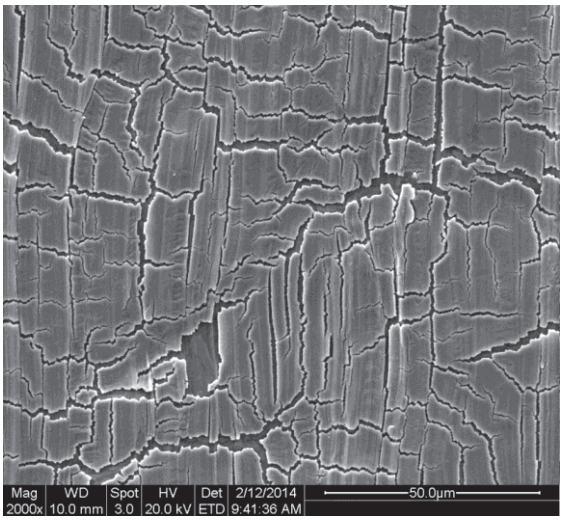

Figure 6.13: Top-view of 8% biaxially deformed, 0.2mm thick, coated, unexposed sample, 2000x magnification, SE accelerating voltage 20kV.

Figure 6.14 presents the SEM image of the biaxially deformed sample after 6 minutes of exposure in 2000x magnification. The coating has developed an oxide as the edges of the cracks are smoother. That is due to the rapid oxidation of cobalt transforming the metallic Co coating into Co_3O_4 [21]. This is supported by the oxygen signal in the EDX maps (Figure 6.15) showing that the areas of the coating, are now rich in oxygen. The area of the cracks seems to be rich in chromium and iron, while the absence of oxygen suggests that the oxide formed on the uncoated surface in the cracks is extremely thin after 6 min of exposure.

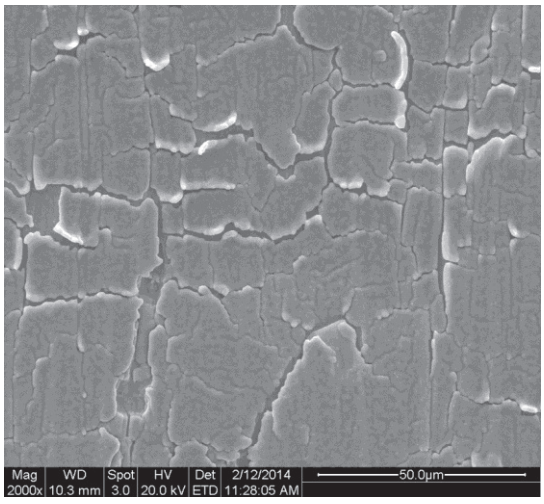

Figure 6.14: Top-view of 8% biaxially deformed, 0.2mm thick, coated sample after 6 minutes of exposure, 2000x magnification, SE accelerating voltage 20kV.

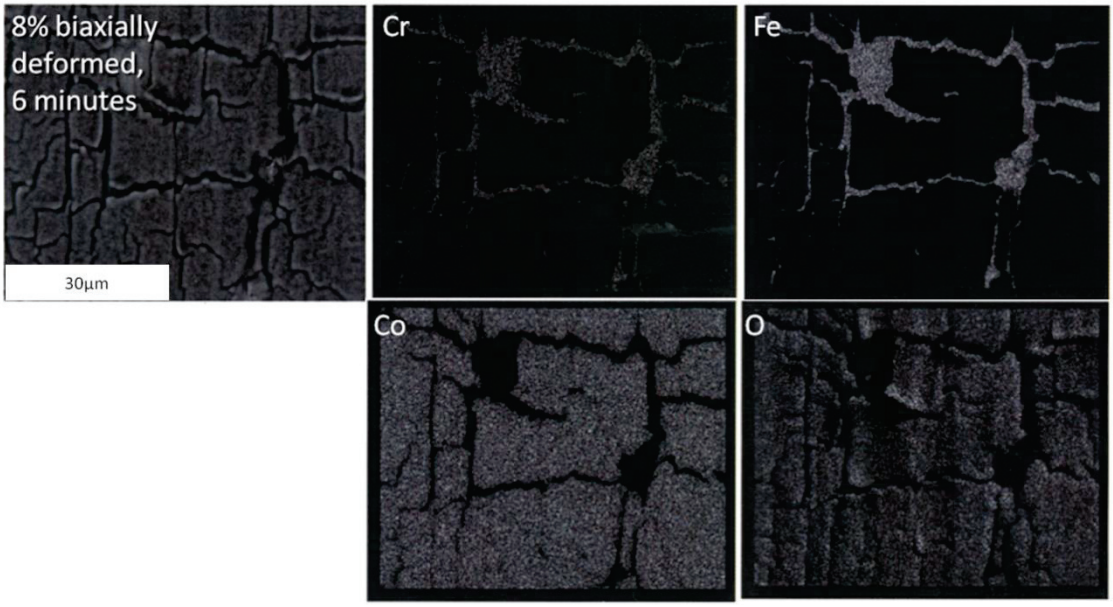

Figure 6.15: EDX maps for the 8% biaxially deformed, 0.2mm thick, coated sample after 6 minutes of exposure, accelerating voltage 20kV.

After 24 hours of exposure (Figure 6.16), the biaxially deformed sample seems to have developed a thin oxide layer within the cracks. According to the EDX maps in Figure 6.17, the much lower iron signal and increased chromium signal within the cracks suggests that a chromium rich oxide been developed there. Iron, however can still be identified at the lines of the cracks, which is probably from the metal due to the thin composition of the chromia layer. Additionally, the presence of manganese in the cracks suggests the formation of an upper $(Cr,Mn)_3O_4$ spinel type oxide according to earlier studies of uncoated AISI 441 exposed in the same environment and temperature [20]. Manganese is also visible on the area of the coating, which is due to its outward diffusion and enriching of the outer cobalt spinel. The growth of the cobalt oxide layer also extends within the cracks, thus explaining the presence of cobalt in the cracks.

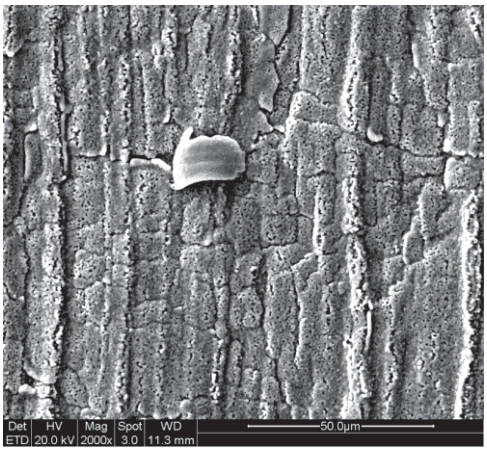

Figure 6.16: Top-view of 8% biaxially deformed, 0.2mm thick, coated sample after 24 hours of exposure, 2000x magnification, SE accelerating voltage 20kV.

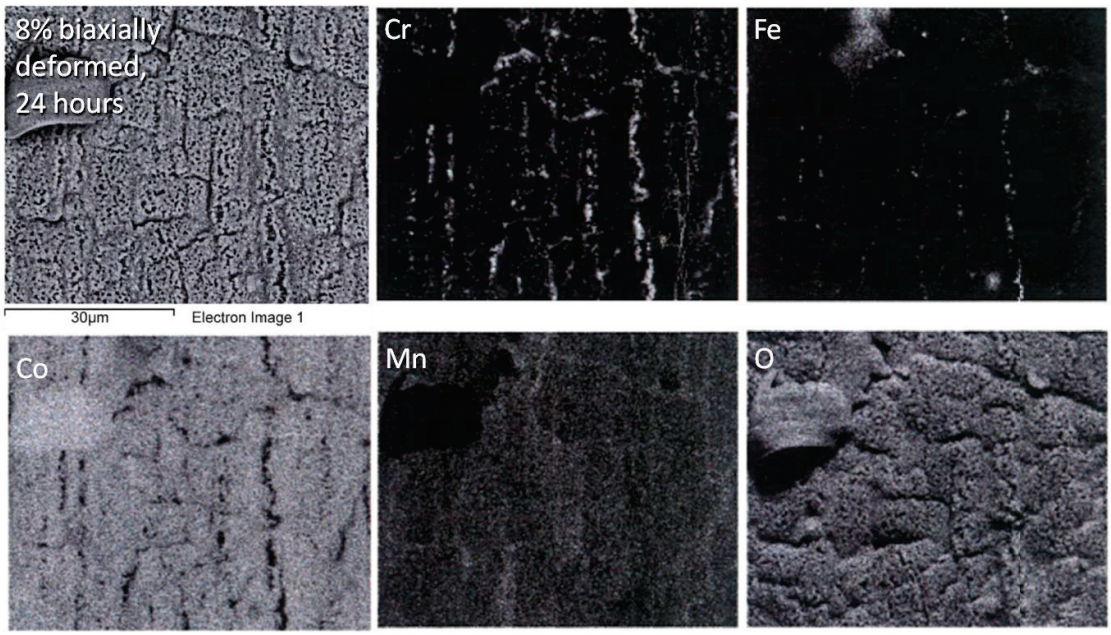

6.17: EDX maps of the 8% biaxially deformed, 0.2mm thick, coated sample after 24 hours of exposure, accelerating voltage 20kV.

Figure 6.18 presents the biaxially deformed samples after exposures of 168 h and 336 h of exposure. After 168 h of exposure, the surface is covered by a uniform, well adherent oxide layer and the cracks were no longer visible. The EDX maps in Figure 6.19 indicate that after 336 h the surface is rich in cobalt and manganese suggesting that most of the surface is covered by $(Co,Mn)_3O_4$. However, along the rolling direction of the steel, a considerable amount of chromium was detected with EDX with an accelerating voltage of 20kV. That can be attributed to the fact that the Co oxide could be thin locally and the high accelerating voltage penetrated the top layer. As seen in Figure 6.5, there was no increase in Cr evaporation. Additionally The Cr rich areas show a random appearance in comparison with the biaxially deformed samples, where a clear pattern is observed along the rolling direction of the steel sheet, as seen in Figure 6.19.

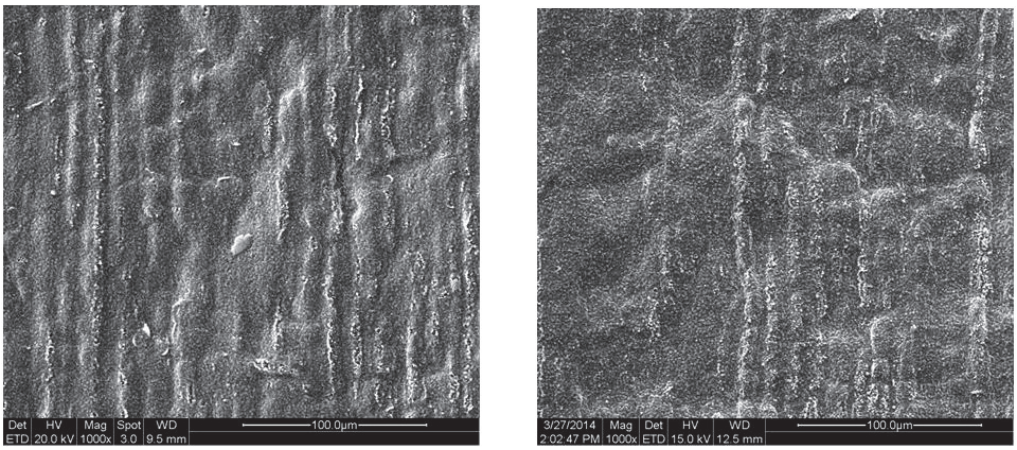

Figure 6.18: Top-view of 8% biaxially deformed, 0.2mm thick, coated sample after 168 hours and 336 hours of exposure, 2000x magnification, SE accelerating voltage 20kV.

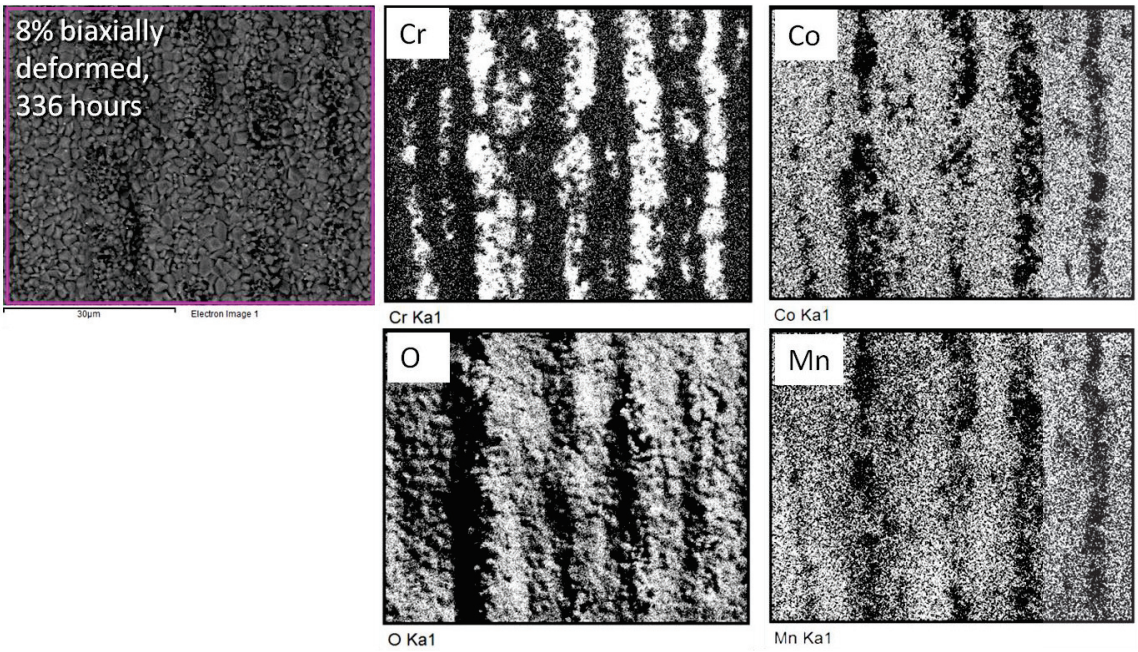

Figure 6.19: EDX maps of the 8% biaxially deformed, 0.2mm, coated sample after 336 hours of exposure, accelerating voltage 20kV.

6.3.4. Coated, Interconnect shaped samples.

In Figure 6.20 the unexposed, 0.3mm thick, interconnect shaped sample can be seen at 200x and 1000x magnification. The cracking of the coating is similar to the biaxial deformation, as shown in chapter 6.3.3. Compared to the 8% biaxial deformation of the 0.2mm thick 441 steel, the cracks seem to be wider in thickness and one can see that the coating has spalled off at several places. The EDX maps of the unexposed, coated interconnect in Figure 6.21 indicate that the cracks are rich in Cr and Fe, as they present the composition of the 441 steel, while the areas where the coating is present are rich in Co.

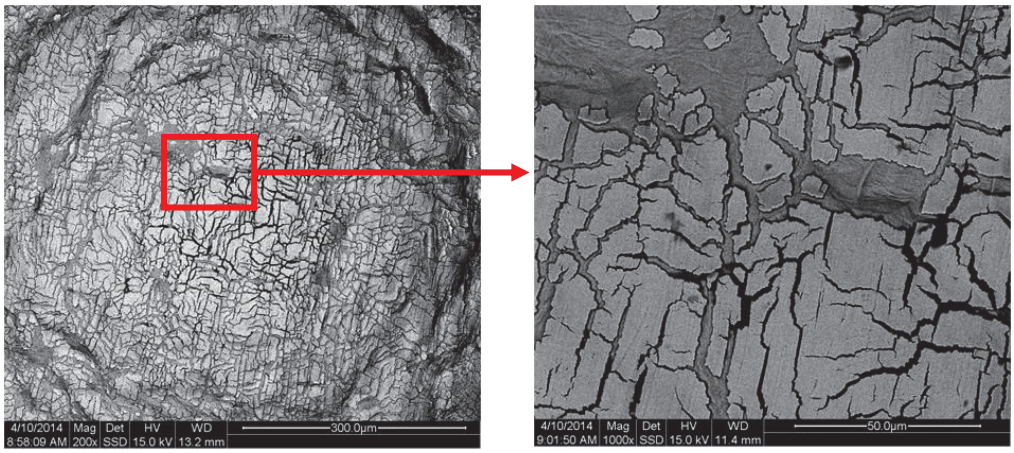

Figure 6.20: Top-view of interconnect shaped, 0.3mm thick, coated, unexposed sample; 200x and 1000x magnification, BSE accelerating voltage 15kV.

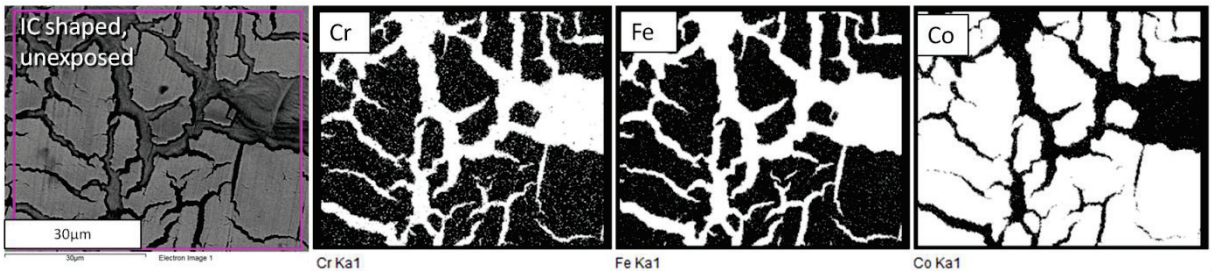

Figure 6.21: EDX maps of the Interconnect shaped, 0.3mm thick, coated, unexposed sample.

After 336 hours of exposure, the interconnect shaped sample has developed a uniform and well adherent oxide layer, as seen in Figure 6.22 at 200x and 1000x magnification. The EDX maps (Figure 6.23), produced with accelerating voltage 15kv, indicate that after 2 weeks the surface is rich in Co and Mn suggesting that most of the surface is covered by $(Co,Mn)_3O_4$. However, as was also observed in the EDX maps of the 8% biaxially deformed samples, areas richer in chromium were detected.

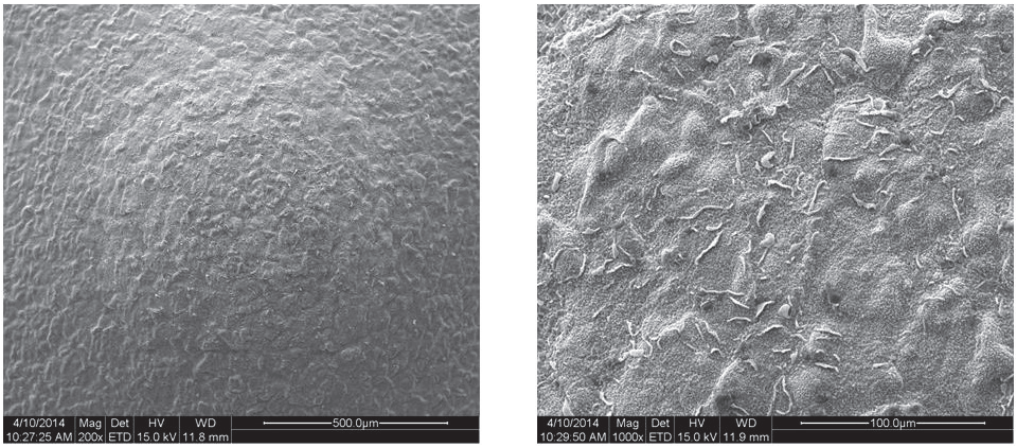

Figure 6.22: Top-view of interconnect shaped, 0.3mm thick, coated sample after 336 h of exposure; 200x magnification, SE accelerating voltage 15kV.

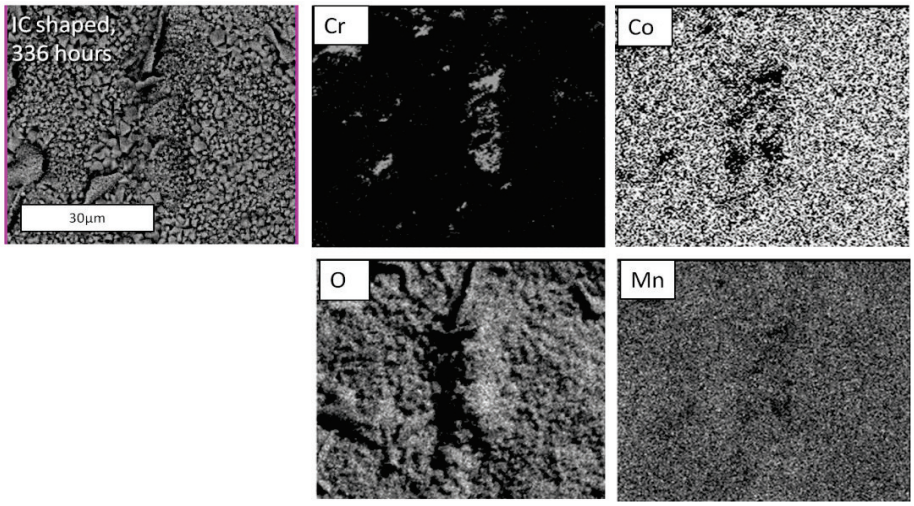

Figure 6.23: EDX maps of the Interconnect shaped, 0.3mm thick, coated sample after 2 weeks of exposure, , accelerating voltage 15kV.

6.3.5. Coated, uniaxially deformed samples.

Figure 6.24, presents the morphology of the cracks on the coated, 0.3mm thick, unexposed samples after 10%, 20% and 28.1% uniaxial strain, at 2000x magnification. The cracks seem to follow a uniaxial direction and their width tend to increase from 10 to 20% strain but no clear difference was observed due to further increased strain.

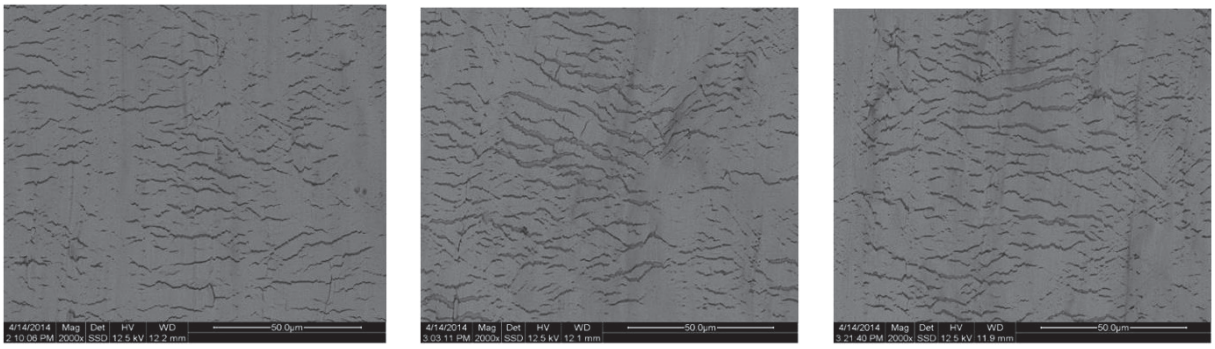

Figure 6.24: Top-view of 10%, 20% and 28.1% (left to right) uniaxially deformed, 0.3mm thick, coated, unexposed sample; 2000x magnification, BSE accelerating voltage 12.5kV.

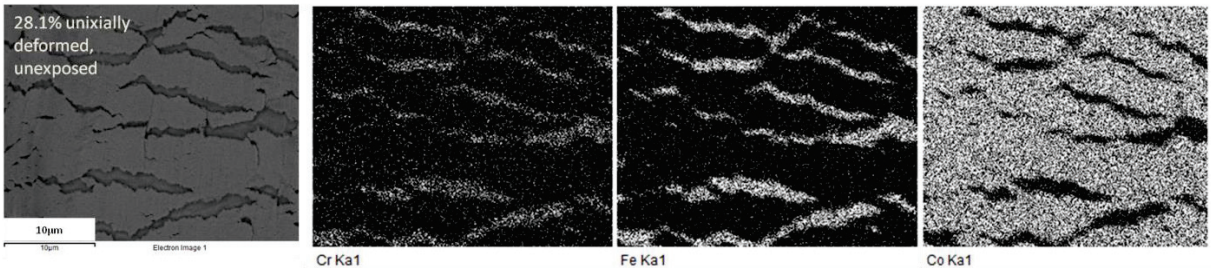

Figure 6.25: : EDX maps of the 28.1% uniaxially deformed, 0.3mm thick, coated, unexposed sample, accelerating voltage 15kV.

In Figure 6.26, the top view of the 28.1% uniaxially deformed sample is presented after 336 h of exposure. The oxide layer seems uniform and well adherent. The EDX maps, produced with a accelerating voltage of 20kV (Figure 6.27) shows that the surface is rich in Co and Mn suggesting that most of the surface is covered by $(Co,Mn)_3O_4$. Similarly to the biaxially deformed and interconnect shaped samples, Cr is detected. The uniaxially deformed sample presents Cr-rich areas with a random pattern which could not directly be correlated to the cracks formed during the deformation process, as seen in the case of the IC and biaxially deformed samples.

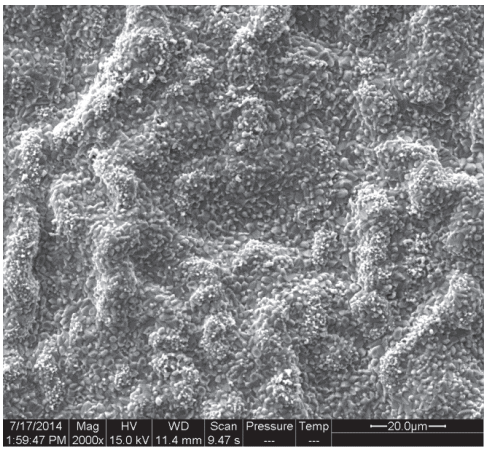

Figure 6.26: Top-view of 28.1% uniaxially deformed, 0.3mm thick, coated sample after 336 hours of exposure; 2000x magnification, SE accelerating voltage 15kV.

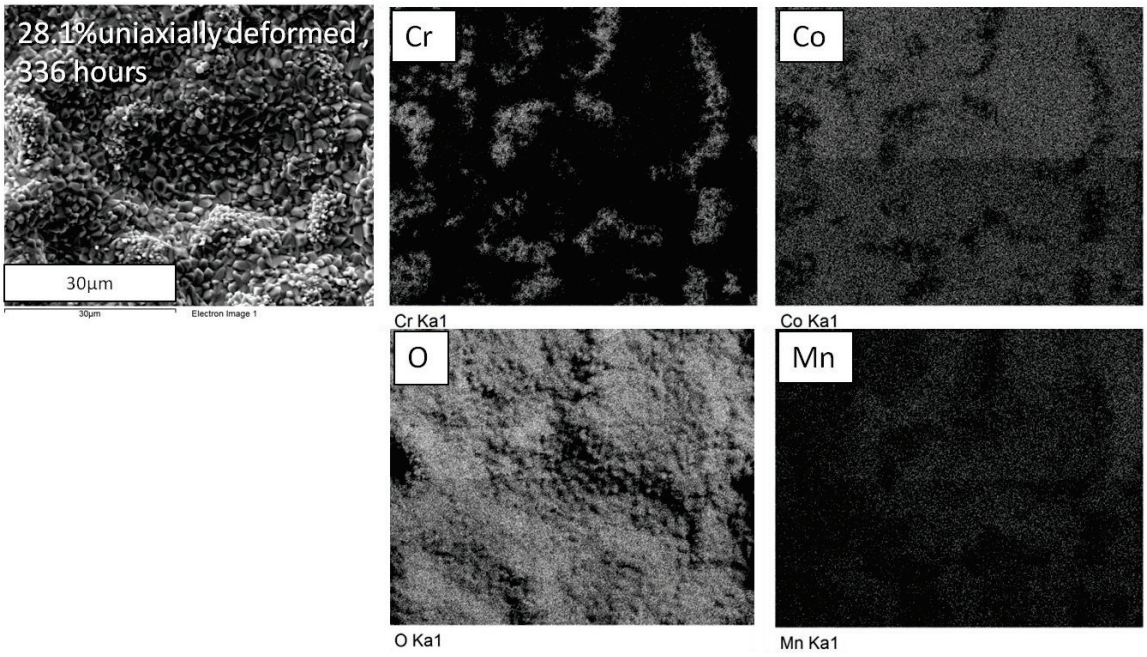

Figure 6.27: EDX maps of the 28.1% uniaxially deformed, 0.3mm thick, coated sample after 336 hours of exposure, accelerating voltage 15kV.

7. Discussion

7.1. Mass gain

The oxidation behavior of the samples has been assessed via gravimetric analyses. The samples' mass gain was plotted for isothermal exposures up to 336 h. All coated samples exhibited the same, almost parabolic rate law behavior. Long term exposures were performed for the interconnect-shaped samples for up to 2132 h. Both the coated and the uncoated ones followed an almost parabolic rate law. The uncoated samples, exhibited a considerable amount of spallation, specifically after 200 h, where the maximum drop in mass gain is observed. After approximately 200 h of exposure the mass gain for the uncoated and the coated sample was the same. After 200 h of exposure, the uncoated sample showed a somewhat lower mass gain value than the coated samples. The lower mass gain for the uncoated sample is assumed to be related to spallation of the oxide scale as well as the significantly higher amount of Cr vaporization. Except the rapid initial oxidation of the Co-coating, the uncoated material showed a much faster gain in mass during the first 200 h of exposure. The slower mass gain for the coated sample compared to the uncoated is assumed to be due to the Ce coating of the coated samples. Earlier studies with 10nm Ce coatings have shown a clear beneficial effect of thin Ce coating [22], probably due to slower ionic transport through the oxide scale. The three samples that were exposed simultaneously in every case, showed negligible deviation in the mass gain, thus the error bars in the coated samples are not visible in the figures. The uncoated samples on the other hand, showed a considerable deviation due to spallation of the oxide scale.

7.2. Cr volatilization

Regarding Cr evaporation were plots produced for all samples with data gathered during the isothermal exposures. The accumulated evaporated chromium for all coated materials showed little difference compared to the evaporated Cr from the uncoated sample after 336 h of exposure. Among the coated samples, the biaxially deformed sample presented the lowest Cr evaporation assumingly due to its smaller thickness (0.2 mm compared to 0.3 mm for the other samples). A 0.2 mm thickness corresponds to 2.59 % uncoated surface whereas 0.3mm corresponds to 3.84%. The uniaxially deformed and interconnect shaped samples lie approximately at the same levels. Cr evaporation measurements on the samples oxidized for 2132 h (the interconnect shaped samples) show a higher Cr evaporation rate for the uncoated sample and approximately the same rate for the coated samples compared to after 336 h of exposure. One could argue that the large variation in collected chromium species for the uncoated long term samples could be due to spallation leaving an open Cr-rich surface which then heal by forming a $(Cr,Mn)_3O_4$ top layer again. The reason for the generally higher rate of Cr.-vaporization could be related to the rather low Mn content in the steel. During the long term exposure spallation took place hence $(Cr,Mn)_3O_4$ was continuously lost. The amount of Mn in the steel is very low (0.26 %wt) hence not enough Mn may be present in the steel to form a new, continuous $(Cr,Mn)_3O_4$ top layer. In the case for the coated steel, the rate is constant during the exposure. The isothermal 336 h exposure indicates that the rate of Cr vaporization did actually slightly increase during the exposure to approximately the same level as the samples exposed for 2132 h. That could be supported by investigating the presence of Cr during the evolution of the top layer of the biaxially deformed samples in the EDX maps after 6 minutes, 24 and 336 hours of exposure in Figures 6.15, 6.17 and 6.19 respectively. With time, more Cr can be detected on, or closely underneath, the surface of the sample. Thus its volatilization is consequently increased over time. It should however be pointed

out that these Cr richer areas could not be correlated to the cracks formed during the mechanical deformation process.

7.3. SEM

15-20 kV accelerating voltage was used hence Cr signals from up to approximately 1μm depth could be detected. All coated samples have proven to form a uniform and well adherent oxide layer after 336 h of exposure. The EDX maps identified the existence of mainly Co and Mn oxide on the surface, which indicates that the top layer is mainly comprised of $(Co,Mn)_3O_4$. However, areas rich in Cr were also detected in all coated samples after 336 h of exposure. At the areas where Cr was mostly identified, Mn and Co were poorer. Specifically in the case of biaxial deformation, the Cr signals were more profound. As shown in Figure 5.3, X-rays can be generated from a large interaction volume, compared to the other signals (SE, BSE). That means that the beam can penetrate the top layer and identify elements of the underlying layer, depending on the accelerating voltage of the beam. In the case at hand, the identified Cr could either be on the surface or underneath a relatively thin CoMn spinel. However, due to the low Cr vaporization of biaxially deformed samples but at the same time strong Cr signal along the rolling direction it is assumed that the detected Cr lies underneath the CoMn spinel and not on the surface.

7.4. Proposed mechanism

In Figure 7.1, the proposed mechanism is presented.

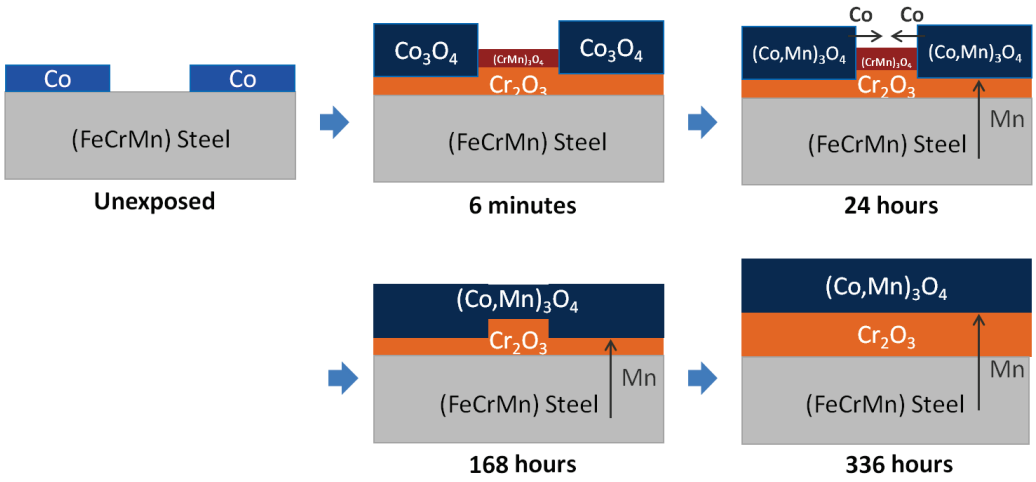

Figure 7.1 The proposed mechanism of crack healing over time (two weeks)

The mechanism regarding the growth of the oxide scale is proposed based on the SEM pictures, EDX mapping and the numerical data that was gathered for Cr evaporation and mass gain. In Figure 7.1, the steel at its unexposed state shows a crack and the metallic cobalt that surrounds it. Upon 6 minutes of exposure, the rapid oxidation of cobalt is observed, while at the crack a thin $(Cr,Mn)_3O_4$ layer is suggested by the presence of Mn in the EDX maps and literature from a similar steel exposed for 1 hour in the same environment [21]. Underneath the Co oxide and at the crack a layer of Cr_2O_3 is also observed. After 24 hours of exposure Mn has diffused out from the steel to the Co-oxide forming a $(Co,Mn)_3O_4$ top layer. Meanwhile, Co is proposed to diffuse from the $(Co,Mn)_3O_4$ to the area of the crack, thus making the crack thinner. After one week of exposure, Mn continues to diffuse towards the outer spinlel layer which covers the area of the crack. By that time the cracks are shown to have healed.

Upon further exposure, after two weeks, the chromium oxide is supposed to continue growing, while a uniform top CoMn spinel has covered the area where the crack was before exposure.

8. Conclusions

The 30nm Ce + 600nm Co coating that was used for this study proved to decrease the Cr evaporation approximately 6 times after 336 hours (2 weeks) compared to the uncoated steel. That is attributed to the presence of Co, which upon exposure at high temperature forms a protective Co-Mn spinel at the surface of the oxide in place of the Cr-Mn that is usually formed on the surface of the uncoated material. Previous studies have illustrated that pure Ce coatings fail to hinder Cr volatilization. However, reactive element coatings have shown to improve the oxidation resistance of the material, as well as provide good adherence of the oxide scale to the metal substrate. Hence, a combination of a duplex Ce/Co coating is a promising one, capable of both reduction of Cr evaporation and improvement in oxidation resistance.

In this study, real interconnect shaped pre-coated samples were investigated. In order to further compare these data to more controlled deformation methods, uniaxially and biaxially mechanically deformed pre-coated samples at different strain levels were investigated. The results showed that the cracks heal within 336 hours of exposure and it is concluded that the cracking of the coating do not have any effect on Cr volatilization. SEM top views showed a uniform and well adherent oxide scale and EDX elemental maps suggested that the surface oxide was rich in Co and Mn, hence, supporting the self-healing phenomenon of the top Co oxide. Finally, a self-healing mechanism has been proposed for the first two weeks of exposure at 850°C.

The investigation on Ce/Co coated AISI 441 steel, has led to the conclusion that a more economical alloy with the above duplex coating can be a promising candidate for SOFC interconnect application. The cost of the interconnects plays a significant role in the total cost of the SOFC stack. The lowering of the cost can thus strengthen the competitiveness of SOFCs in the market.

Further research is aimed at the microstructural investigation of the self-healing mechanism by means of cross sections analyses. Furthermore, in this study, the thickness of all investigated samples was 0.3 mm except for the 8% biaxially deformed ones and presented some expected differences regarding Cr evaporation. A 0.3 thick Ce/Co coated biaxially deformed AISI 441 steel has to be investigated in order for uniformity reasons.

References

[1] J.H. Hirschenhofer, D.B. Strauffer, R.R. Engleman, M.G. Klett. Fuel cell handbook, Fourth Edition. November 1998

[2] J. Larminie, A. Dicks. Fuel Cell Systems Explained, Second Edition. 2003

[3] M. Powell, K. Meinhardt, V. Sprenkle, L. Chick, and G. McVay, *Demonstration of a highly efficient solid oxide fuel cell power system using adiabatic steam reforming and anode gas recirculation.* Journal of Power Sources, 2012. **205**: p. 377-384.

[4] H.F. Windisch, J.E. Svensson, J. Froitzheim. Chromium evaporation from mechanically deformed pre-coated Crofer 22 APU. Proceeding of the 11th European SOFC and SOE Forum, Chapter 08. July 2014

[5] U. Bexell, M. Schuicky, H. Ravash, J. Froitzheim, J.E. Svensson. Chromium evaporation from plastically deformed pre-coated Sandvik Sanergy HT 22% Cr ferritic interconnect steel. Proceeding of the 9th European SOFC Forum, Chapter 12. 2010

[6] J. Froitzheim, H. Ravash, E. Larsson, L.G. Joahnsson, J.E. Svensson. Investigation of chromium volatilization from FeCr interconnects by a Denuder Technique. J Electrochem Soc., 2010.

[7] J.G. Grolig. Coated ferritic stainless steels as interconnects in Solid Oxide Fuel Cells. Licenciate thesis of engineering. 2013

[8] P. Alnegren. Oxidation behavior of selected FeCr alloys in environments relevant for solid oxide electrolysis applications. Master thesis, 2012 [[p11]]

[9] S.M. Haile. Fuel cell materials and components. Acta Materiala, 51(19):5981-6000, 2003

[10] R. M. Ormerod. Solid oxide fuel cells. Chemical Society Reviews, 32(1):17-28, 2003

[11] Neil Birks, Gerald H. Meier, and Frederick S. Pettit, *Introduction to the High-Temperature*

[12] Neil Bricks, Gerald H. Meier, Fredericks S. Pettit. "*Introduction to the High-Temperature Oxidation of Metals*". Second edition, Campbridge university press, 2006

[13] Per Kofstad. *High Temperature Corrosion*. Elsevier Applied Science, 1988.

[14] M. Hasegawa, *Chapter 3.3 – Ellingham Diagram.* Treatise on Process Metallurgy: Process Fundamentals, 2014. **1**: p. 507–516.

[15] B. A. Pint. Progress in understanding the reactive element effect since the whittle and stringer literature review.

[16] D. P. Whittle and J. Stringer. Improvements in high-temperature oxidation resistance by additions of reactive elements or oxide dispersions. Philosophical Transactions of the Royal Society of London Series a-Mathematical Physical and Engineering Sciences, 295(1413):309{&, 1980.

[17] B. B. Ebbinghaus. Thermodynamics of gas-phase chromium species – the chromium chlorides, oxychlorides, uorides, oxyuorides, hydroxides, oxyhydroxides, mixed

[18] H. Ravash. Chromium Volatilization and Oxidation of Ferritic Steels Used as Interconnects in Solid Oxide Fuel Cells, 2010

[19] J. Froitzheim and J. E. Svensson. Multifunctional Nano-Coatings for SOFC Interconnects, volume 35 of ECS Transactions, pages 2503{2508. 2011

[20] J.G. Grolig, J. Froitzheim, J.E.Svensson. Coated stainless steel 441 as interconnect material for Solid Oxide Fuel Cells: Oxidation performance and chromium evaporation. Journal of Power Sources, 2013

[21] J. Froitzheim, S. Canovic, M. Nikumaa, R. Sachitanand, L.G. Johansson, L.E. Svensson. Long term study of Cr evaporation and high temperature corrosion behaviour of Co coated ferritic steel for solid oxide fuel cell interconnects. Journal of Power Sources 220 (2012) 217-227.

[22] S. Canovic, et al., *Oxidation of Co- and Ce-nanocoated FeCr steels: A microstructural investigation.* Surface and Coatings Technology, 2013. **215**(0): p. 62-74..

[23] Matthew P Dewar. Characterization and evaluation of aged 20cr32ni1nb stainless steels. Master's thesis, University of Alberta, 2013.

[24] K. L. Scrivener. Backscattered electron imaging of cementitious microstructures: understanding and quanti_cation. Cement & Concrete Composites, 26(8):935{945, 2004}